Development of Ultra High Energy Density Heat Sources and Their Application to Heat Processing †

Yoshiaki ARATA*

Abstract

This paper presents studies on the ultra high energy density heat sources, their characteristics and applications to heat processing.

After some historical review of the various types of electron and laser beam equipment, the important problem of focusing large output lasers and electron beams is discussed, together with their characteristics as heat sources.

Moreover, the basic weld zone characteristics produced by ultra high energy density beams are also examined, paying particular attention to hardness and the "Fracture Path Transition Temperature".

Finally, the author refers to the experimental results of horizontal electron beam welding, Tandem Electron Beam Welding and laser beam welding, and describes the similarities and differences in processing characteristics of the laser beam and electron beam.

KEY WORDS: (High Energy Density Beam) (Heat Source) (Laser Welding) (Electron Beam Welding) (Heat Processing)

1. Introduction

Any currently known form of energy, including electromagnetic energy, mechanical energy and chemical reactive energy can be employed as a heat source for practical use such as for heat processing.

A wide variety of manufacturing heat sources are available through various technologies, but from the practical viewpoint they can be studied basically by generalizing the problem to two major points of their power and density.

In conventional studies on energy and heat source problems, considerable advances have been made in research on grades of energy, power magnitudes and their applicability, but it seems that not as much research has been devoted to the question of energy density and control.

Recently, however, electromagnetically accelerated particle beams such as electron, ion, neutral and special type plasma beams with large outputs have been developed. These beams have inherently high energy density and have begun to be used as high energy density heat sources. Heat sources of such large output and high density are capable of opening up new applications in the future, particularly if employed for processing and will not only contribute greatly to industry but will also help to develop new areas of science and technology.

High energy density beams can be produced in either a pulsed or continuous mode. However, to utilize them more widely as a popular heat sources such as the arc, they should have outstanding characteristics, particularly with regard to continuous output. From this standpoint we have been endeavoring for over twenty years to develop equipments with a large continuous output and to clarify their characteristics.

We also believe that when considering the laser beam as a processing heat source, it should always be compared with an electron beam or plasma heat source. Thus, we believe that the basic task in utilizing high power lasers is to clarify the characteristics of each heat source and confirm the similarities and differences in processing characteristics. That is why I have selected the electron beam as well as the laser beam in this report, and the study results described later in this paper reflect this orientation.

2. Development of Ultra High Energy Density Beams

Among those who have contributed to the development of electron beam heat sources are Pierce[1], Steigerwald[2], Stole[3], and many other famous researchers. The researchers who helped to develop the laser beam heat source include such celebrated people as Maiman[4], known for the ruby laser; Patel[5], for the CO_2 laser; and Brides[6], for the Ar-ion laser, and other excellent researchers.

I have paid primary attention to the continuously oscillating CO_2 laser beam as a high power heat source for processing. First of all my interest in large output heat sources was triggered in 1957, when we created a pinch plasma using an electric discharge of 1.6 MA for research into nuclear fusion[7]. This was the origin of experimental studies of nuclear fusion in Japan. To obtain an ultra high temperature plasma other than pinch plasma, we planned

to create a large output pulse electron beam, and proposed the "Transtron" accelerator[8], also to be called a linear betatron, and developed the first stage accelerating section[9], as shown in **Fig. 1**. Using this accelerator,
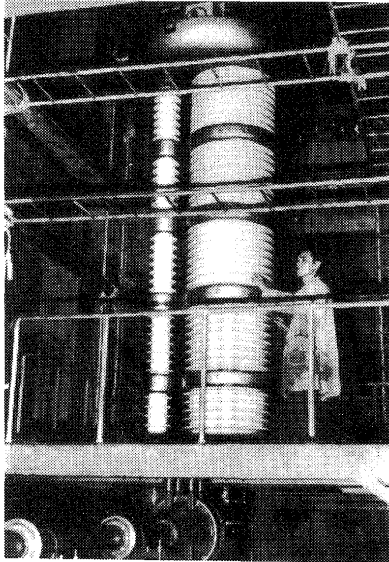

Fig. 1   Transtron Accelerator.

we obtained an energetic beam with a voltage of 1 MV and a current of 260 A using a hot cathode and 300 kV and several thousand amperes using a plasma cathode.

Those are pulse devices and their industrial applications are limited. Thus we found it urgently necessary to develop some large output equipment capable of a continuous output. In 1972 we succeeded in developing the world's first 100 kV, 100 kW electron beam welding device[10] as shown in **Fig. 2**. In 1975 we developed 300 kV, 100 kW
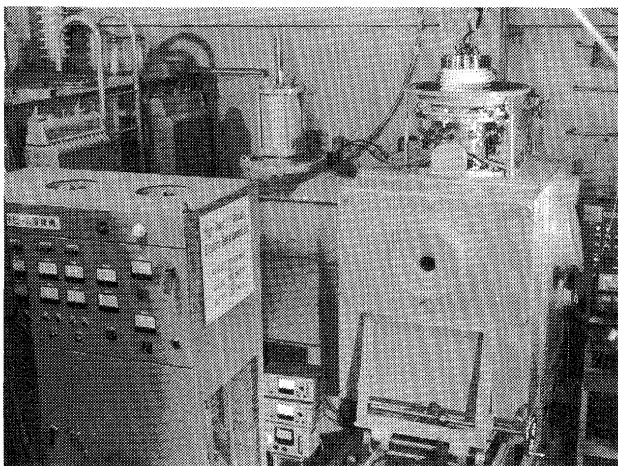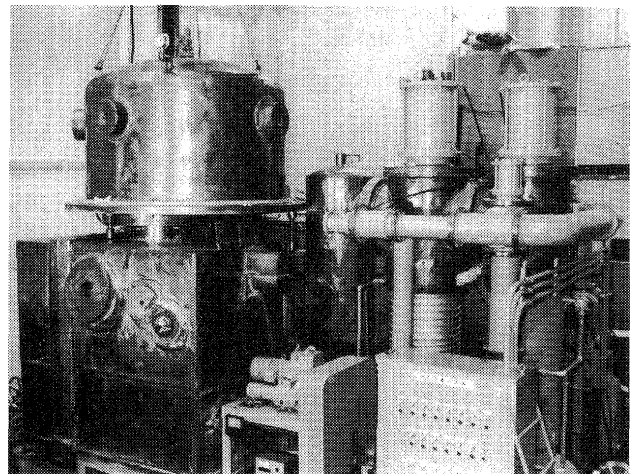

Fig. 2   100 kW 100 kV EB Welder.

device[11] as shown in **Fig. 3 (a)**. In 1980 we produced, by way of experiment, 600 kV, 300 kW electron beam device as shown in **Fig. 3 (b)** for welding etc.[12], having presently the largest output in the world. These devices in **Fig. 3** could be realized by the development of a new
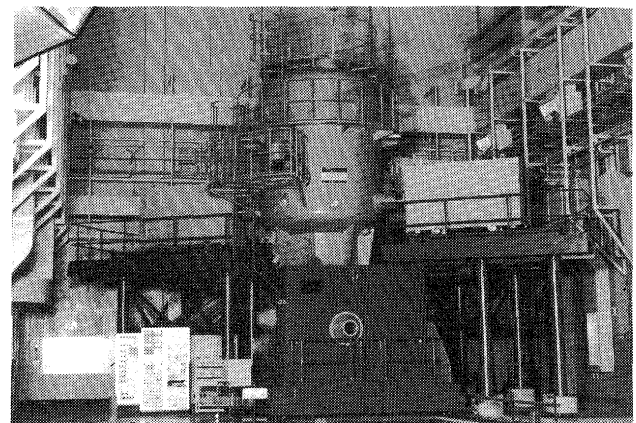

(a) 100 kW 300 kV EB Welder.

Fig. 3   (b) 300 kW 600 kV EB Welder.

acceleration system of "electromagnetic acceleration unit"[13] shown in **Fig. 4**. Using these high power devices, we have established "a new welding method on ultra thick metal plates" of over 30 cm in thickness. Several years later, researches for practical use of such a source began in various countries[14].

A large output CO_2 laser was realized through research carried out by Whitehouse[15], Tifferny[16], Lock[17], Banas[18] and many others. In 1966 we introduced a 1 kW CO_2 laser device shown in **Fig. 5** and developed the world's first large output continuous CO_2 laser welding-cutting method. In particular, the name "laser gas cutting[19] which we gave to the cutting method is now widely used. At about the same time, we developed a different cutting method as shown in **Fig. 6** and named it "electron beam gas cutting"[20]. In terms of its cutting property, the laser beam method seems superior but further detailed study on it will be required in the future. Although in the range of up to 3 kW (1970), we used trial equipment made by ourselves, we are now using 5 kW system made by Spectra-Physics and 15 kW one made by AVCO to carry out research on welding (of metallic or non-metallic
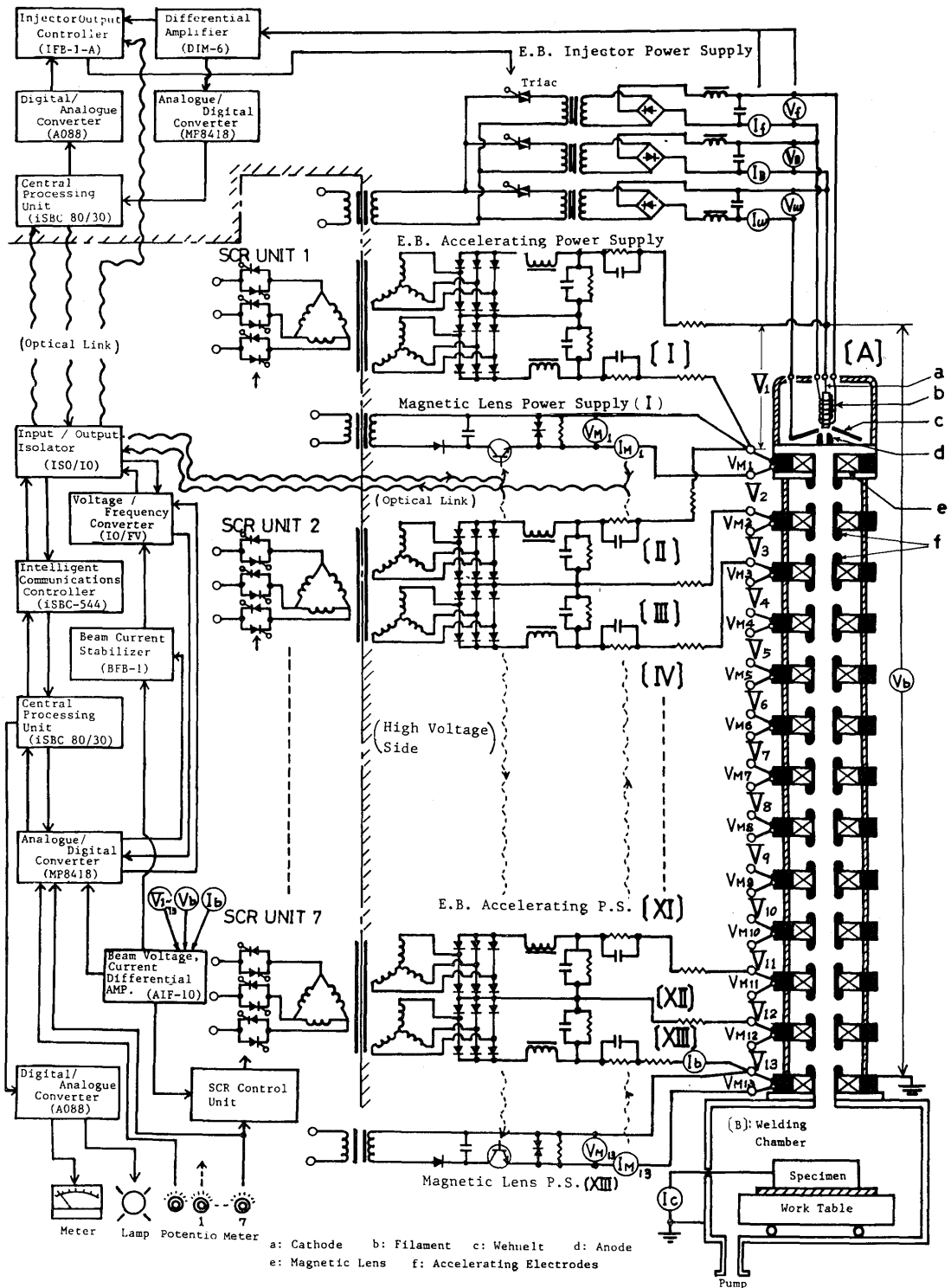
Fig. 4   600 kV–300 kW strong focusing type 13-stage accelerating electron beam heat source.
[A] : EB gun with 13 electromagnetic acceleration unit.

materials (ceramics)[21], cutting, heat treatment (such as, laser surface hardening[22], laser gas hardening[23]) and alloying etc.

Such large output laser and electron beam equipments

have been installed in "The Research Center for Ultra High Energy Density Heat Source" of our institute established in 1980. Other new equipments for high power and high energy density heat sources are also being
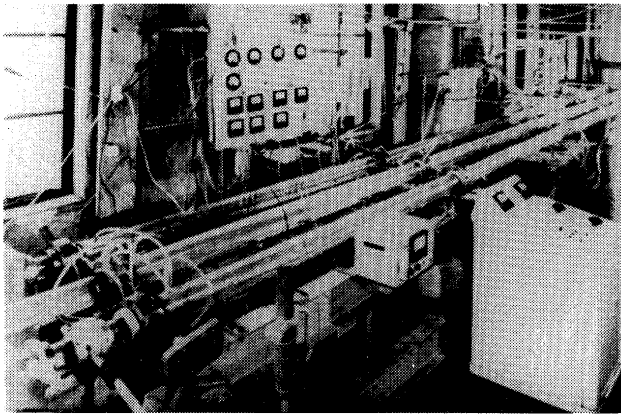
Fig. 5   1 kW CO_2 Laser Welder (and applicable also to cutting). The first CO_2 laser for material processing.

6mm^t SUS304
$V_b = 110KV$
$I_b = 11mA$
$v_b = 10cm/min$

10mm^t Ceramics
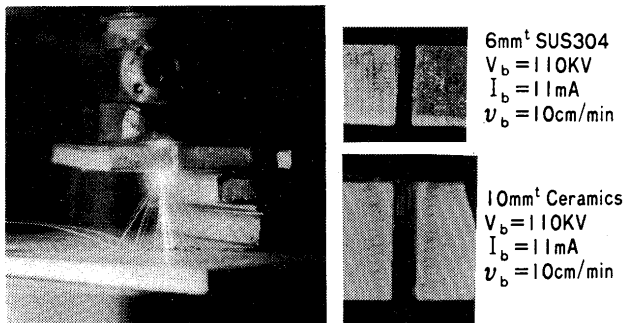$V_b = 110KV$
$I_b = 11mA$
$v_b = 10cm/min$

Fig. 6   NV-EB gas cutting with two samples of the cutting cross section.
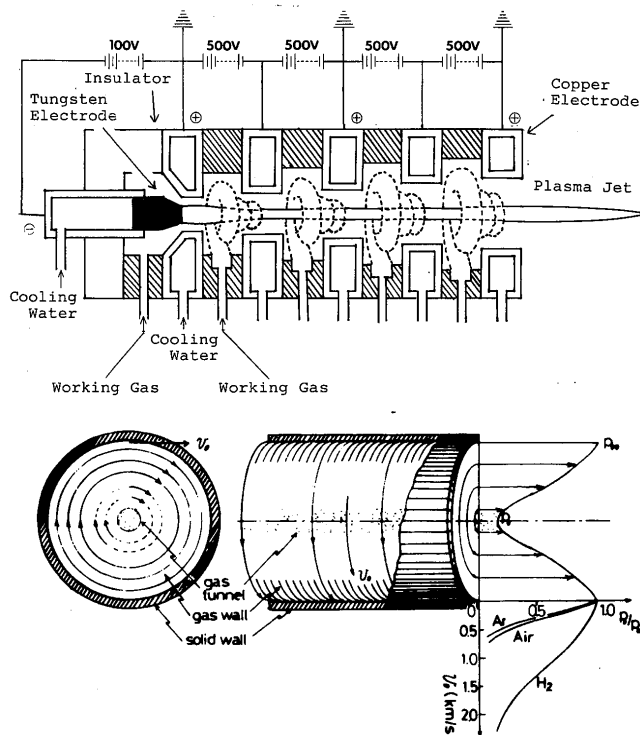

Fig. 7   Principle of the "Gas Tunnel" and its Special High Power Plasma Jet Device.

constructed and researched in this research center. One is a new type of special high power plasma jet device shown in **Fig. 7**. This device can produce a "gas tunnel" of low pressure by using a special strong vortex gas flow[24]. Inside this gas tunnel the pressure reaches a level below 20 Torr. Therefore, a very stable high power arc plasma beam can be created along its axis. By using this device we produced an Argon plasma beam of about 30000 K at 800 A with input power of 150 kW. Another device being developed is the ECR Plasma device shown in **Fig. 8**. Using a 60 GHz,
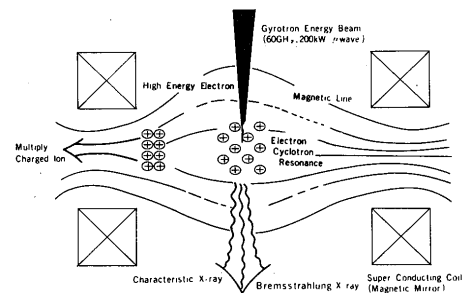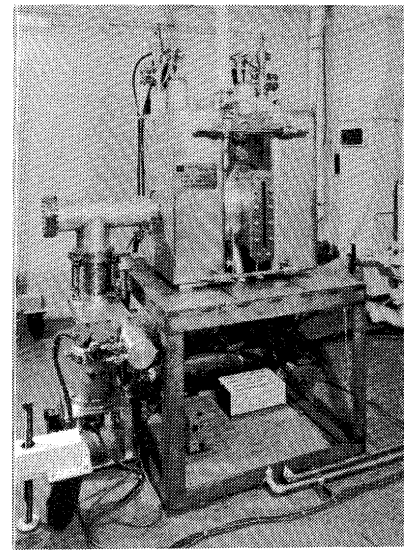

Fig. 8   ECR Plasma Device and its explanation drawing of ECR heating.

200 kW Gyrotron, a high temperature and high density plasma is produced in the magnetic mirror of super conducting magnets by electron cyclotron resonance heating.

3. Fundamental Characteristics of Ultra High Energy Density Heat Sources

Since the degree of energy density obtained from electron beams and CO_2 laser beams is almost identical, their characteristics as a heat source are similar in many respects. However, their processing characteristics differ in considerable cases because their spatial propagation characteristics and their interaction with materials are different.

a) Converging lens focus system. (conventional system) b) Arata laser focus system. c) Parabolic mirror type focuss system.
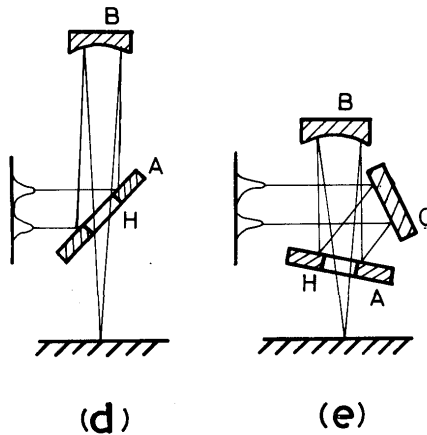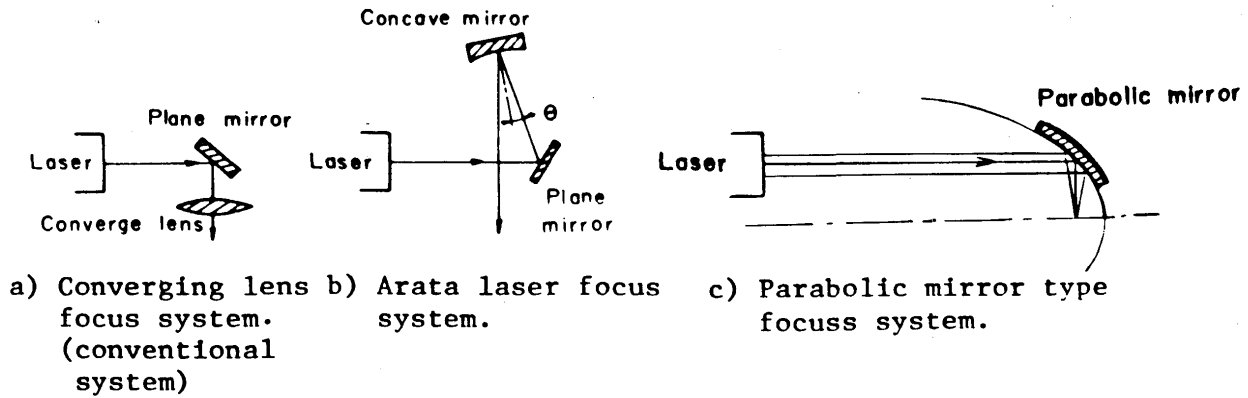

(d)   (e)

Fig. 9   Beam focusing methods. The principle of (d) and (e) is the same as system (b). In order to converge the beam downward, optical system using converging lens, spherical mirror which are combined by a plane mirror can be used.
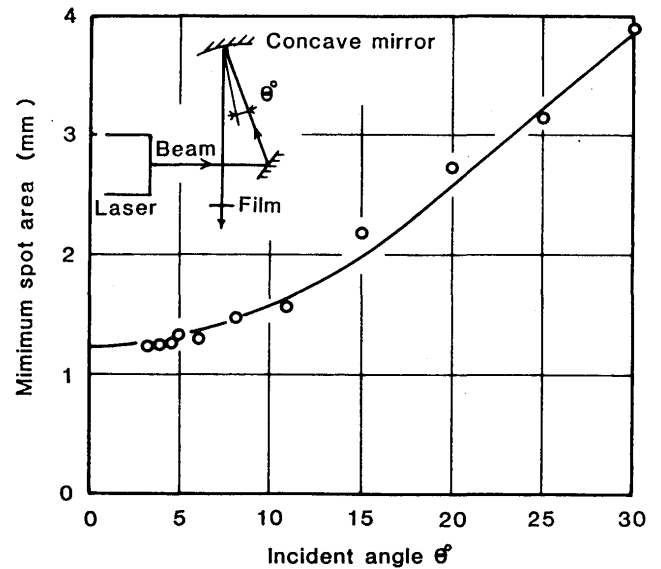
3.1 Focusing

To utilize a laser beam in a state of high energy density, the method of beam focusing is extremely important. **Figure 9** shows five kinds of basic beam focusing systems. Traditionally used are (a) and (c), whereas (b) is the method proposed by the author about 15 years ago as a large output laser focusing method[25],[26]. It is called the Arata laser focus system[27] and its features are shown in **Fig. 10**. The preferred convergence angle should be smaller than a few degrees. Compared with other systems, in this system the greater the laser output the more effective the function becomes. The system of Fig. 9 (b) is suitable for a columnar beam such as a Gaussian beam. For hollow beams, systems (d) and (e) are suitable, whose principal is the same as system (b). Now we use system (e) for 15 kW CO_2 laser device.

The beam focusing, irrespective of whether it's a laser or an electron beam, can be performed as shown in **Fig. 11**. As an important parameter, the author defined the "a_b value" as follows and named it the "beam active

Fig. 10   Minimum spot area vs. incident angle (focal length: 151 mm, beam diameter: 15 mm).

$$a_b = D_O/D_F$$

$$(D_F: \text{focal distance, } D_O: \text{object distance}) \quad (1)$$

parameter"[28],[29]:

With the incident angle represented as θ and the standard deviation at the focusing point as σ, we also set the beam active zone length ℓ_b as follows[30]'

$$\ell_b = 4.46\sigma/\tan \theta \quad (2)$$

which is essential for knowing the beam's characteristics for heat processing.

Any paper in which the a_b value is not clearly written can only be half evaluated or even not evaluated at all as a research paper in some cases. For example, as shown in **Fig. 12**, the beam penetration depth h_p depends greatly on the a_b value in the case of electron beams, and it varies much more violently in the case of laser beams. Moreover, since the laser heat source causes peculiar changes not only to the penetration depth but to the bead shape as shown in **Fig. 13**, we named this specific phe-

$$a_b = \frac{D_0}{D_F}, \quad f_b = \frac{1}{\tan\theta} = \frac{D_F}{b}$$

$$l_b = 4.46\,\sigma / \tan\theta = 4.46\,\sigma f_b$$
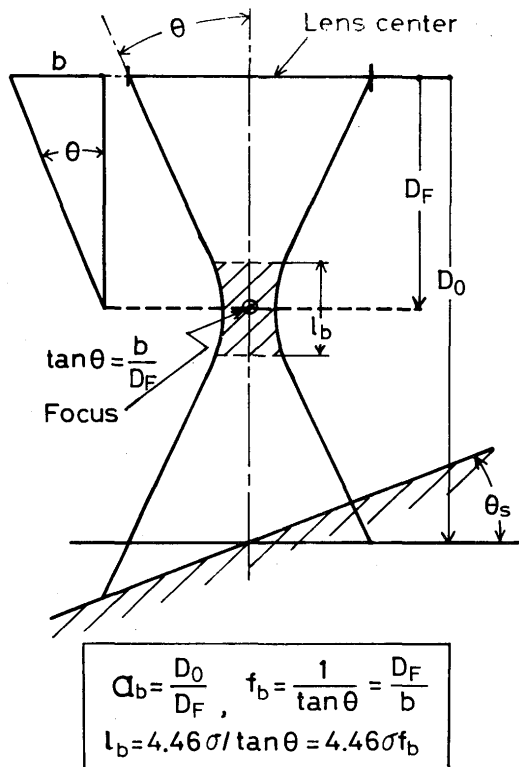
Fig. 11 General view of high energy density beam and its parameters.
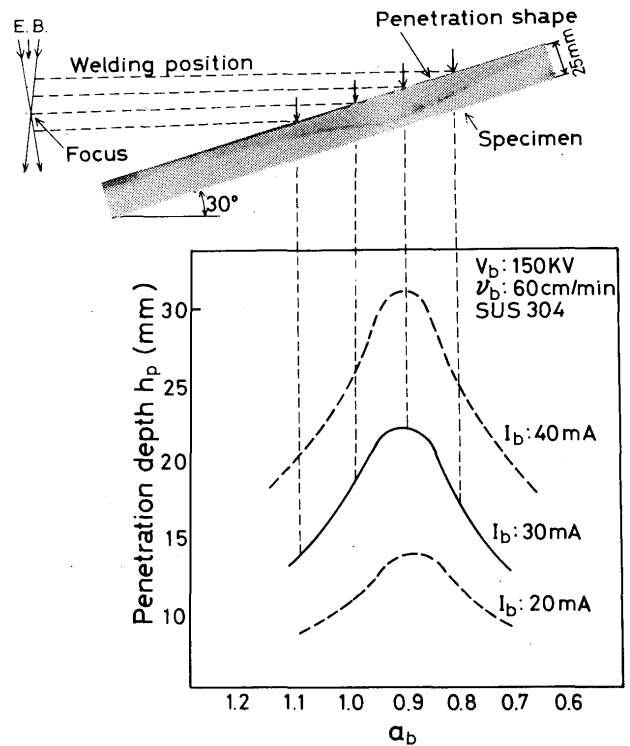
Fig. 12 Relation between active parameter a_b and penetration depth h_p for various current I_b.
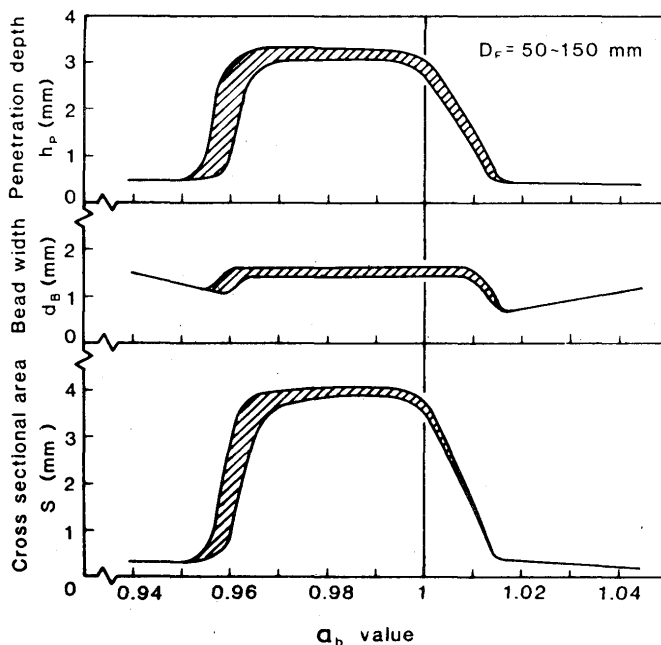
Fig. 13 Relation between a_b value and penetration depth h_p, bead with d_B and cross section S.

nomenon "bead transition"[31]. This is a phenomenon not seen in the case of electron beams. Thus, in utilizing a laser as a heat source at high energy density, the allowable range of a_b values ($\pm\Delta a_b$) is extremely narrow as compared with the case of electron beam (also see **Fig. 14**).

This fact necessitates far higher control in laser welding than in electron beam welding. We have already reported in detail the mechanism of how bead transition is generated[32], so I will not discuss it in this paper.

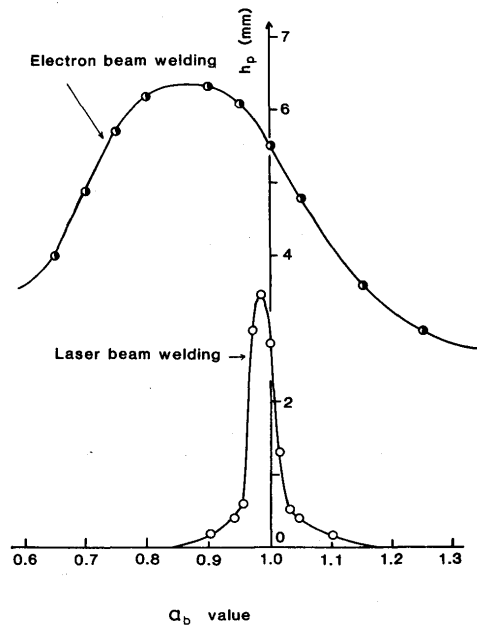So far a number of researchers have proposed shapes
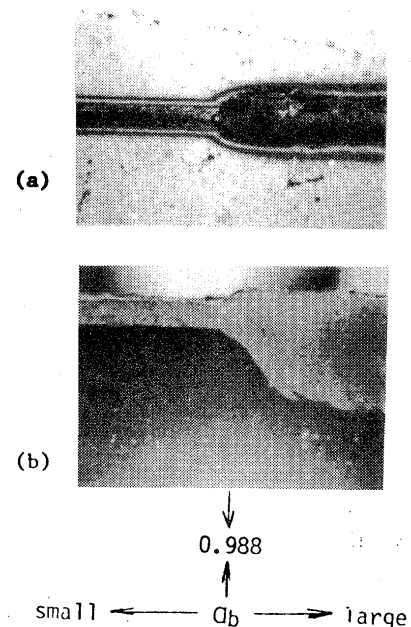
Fig. 14 Comparison of laser welding with electron beam welding for $h_p - a_b$ relation.

of high energy density convergent beams and how to measure their energy densities[33]−[35]. However, their measuring methods are generally complicated and short of accuracy in many cases. Measurement is particularly difficult in the case of large outputs, and even impossible during practical heat processing. The author has proposed a method of measuring the beam shape and mean energy density under such conditions[36],[37]. This method of measurement shown in **Fig. 15**, is now widely used as the
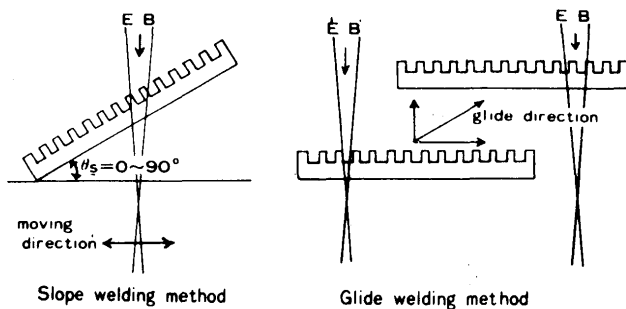

Fig. 15 Schematic drawing of AB test method.

"AB test" (Arata beam test) method[35],[37]. It utilizes the sharp edge effect of a specimen as illustrated, and can be applied to other materials according to output. Ceramics can be used for lasers of not so large an output. **Figure 16** shows an example of an electron beam which is often applied to conventional stainless steel. The beam spot strength $w_b(r)$ in this active zone is normally distributed in a Gaussian form. For example, in the case of a CO_2 laser, **Fig. 17** shows the actual measurements at focus, which are approximated by the Gaussian curve[38]:
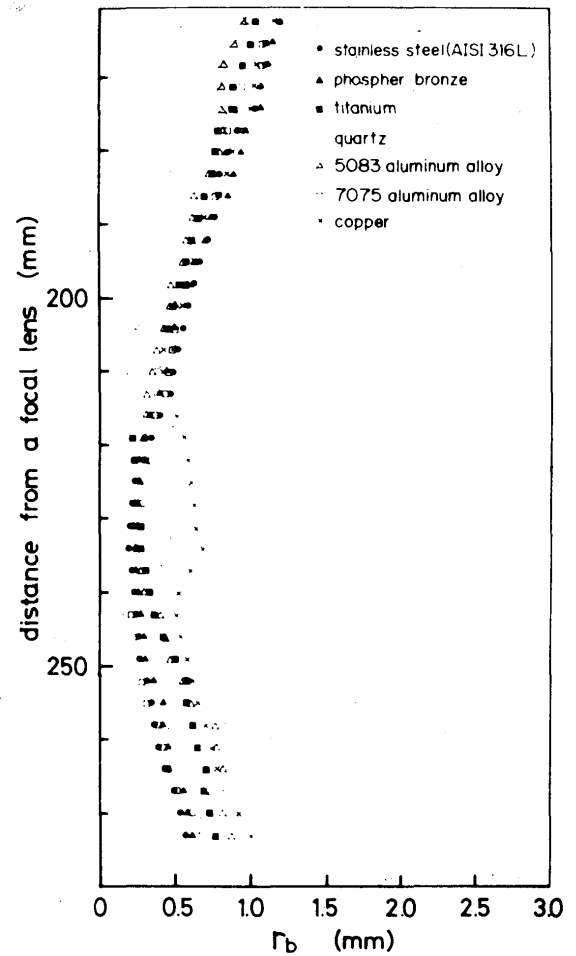

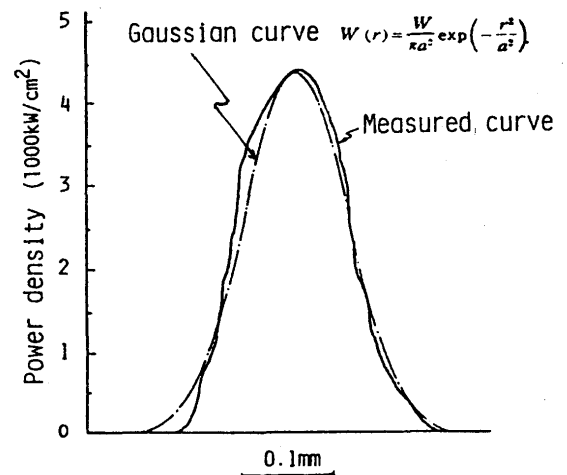Fig. 16 Summarization of proper beam shape for each type of material.

Fig. 17 Power density distribution at focal point.

$$w_b(r) = \frac{W_b}{\pi a^2} \exp\left(-\frac{r^2}{a^2}\right) \qquad (3)$$

where W_b is the beam output, "a" is the beam spot radius and "r" is the distance from the beam axis. In Fig. 17 W_b = 1 kW, $d_b = 2a = 0.17$ mm and its central energy density

is as high as $w_b = 5000\,kW/cm^2$: the focal depth, however, is so small that the energy density decreases by half when separated 1 mm from the focal position ($D_F = 64$ mm). In the case of a multiplex mode of $W_b = 5$ kW, d_b became 0.4 mm and the central density was almost identical to that in the single mode of 1 kW.

The greatest difference between an electron beam and laser beam in terms of heat source characteristics is found in their absorptivity to metal materials. The absorptivity of an electron beam is extremely high, whereas that of a laser is extremely low. This greatly affects the phenomena, and is the most probable cause of the above-mentioned "bead transition". When a CO_2 laser beam was applied to a polished metal surface with a conductivity σ (= $1/\eta$, η: specific resistance), the absorptivity A_b was well compatible with our actual measurements[39] as shown in Fig. 18 using the Hagen-Rubens equation[40].
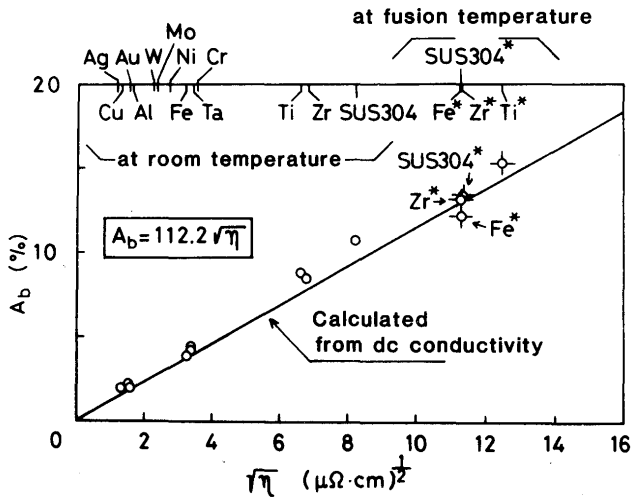

Fig. 18 Absorptivity of metals at room temperature and fusion temperature marked with symbol*. SUS-304 corresponds to AISI 304 stainless steel.

$$A_b = 112.2\sqrt{\eta} \qquad (4)$$

Thus, using these results, we attempted to find the minimum beam power W_{bM} required to heat the metal surface up to the melting point T_M.

$$W_{bM} = 1.58 \times 10^{-2}\kappa d_b T_M\sqrt{\sigma_M} \qquad (a)$$
$$= 8.92 \times 10^{-3}\sqrt{\sigma_M}\,W_{bM}^{*} \qquad (b) \qquad (5)$$

This is shown in Fig. 19. Here W_{bM}^{*} (= $\sqrt{\pi}\,\kappa d_b T_M$) corresponds to W_{bM} at $A_b = 100\%$. As can be understood from Figs. 18 and 19, the absorptivities are less than 15% even in Ti, Zr, Fe, and SUS 304 in the molten state of the highest absorption. This indicates the need for surface treatment to raise the A_b values when metal is to be welded using a laser of several hundred watts. However, if
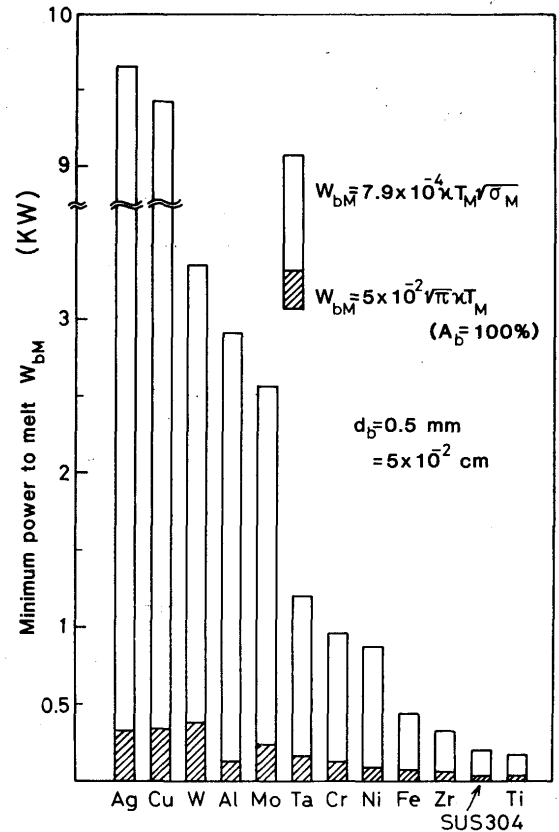

Fig. 19 Minimum laser power to weld various metals with infinite thickness. In this figure σ_M represents dc conductivity at fusion temperature (constant power, Gaussian distribution).

the incident laser beam output W_b increases and the energy density reaches several hundred kW/cm^2, then, as in the case of the electron beam, beam holes will be formed and the beam will make multiple reflections on the wall surface (number of times $N = \pi/\tan^{-1}$ (s/h)). By this phenomenon, laser energy concentrates on the wall and on the bottom as well. We called this phenomenon the "wall-focusing effect"[41],[42]. The laser's effective absorptivity $\tilde{A}_b$ (= W_{bA}/W_b) or absorption beam power W_{bA} rapidly rises due to this effect along with the beam hole depth h_p as shown in the following formula and the illustration in Fig. 20, so these parameters become independent of the state of the material surface.

$$\frac{W_{bA}}{W_b} \;(\equiv \tilde{A}_b) = 1 - (1 - A_b)^{\pi/\tan^{-1}(s/h)} \qquad (6)$$

Here it is assumed that the beam hole is wedge-shaped as shown in Fig. 20, that is, s, h and A_b are the beam inlet width, depth and wall surface absorptivity, respectively, and there is no effect from the plasma, etc. Usually we may assume that $s = d_b$ and $h = h_p$. On the other hand, on the assumption that the beam is a line heat source travelling at speed v_b and that the weld bead width d_B and penetration depth h_p are formed in a material with melt-
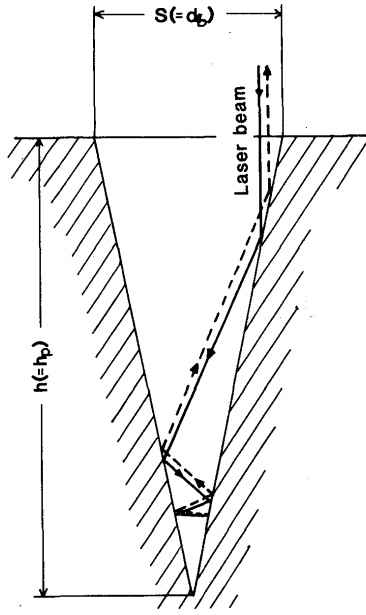
Fig. 20 Reflection path of laser beam in wedge shape cavity.

ing point T_M, thermal conductivity κ and thermal diffusivity κ_D, the beam power W_{bC} required becomes[43]:

$$W_{bC} = 8\kappa T_M \left(0.2 + \frac{v_b d_B}{4\kappa_D}\right) h_p \tag{7}$$

As shown in **Fig. 21**, the above W_{bC} increases in proportion to h_p and intersects the W_{bA} curve ($W_{bC} = W_{bA}$). Thus, the beam hole can grow deep enough to reach the intersection. This is a heat source characteristic of laser beams, which have a large reflection loss, and is one of the main characteristics which differ substantially from electron beams, whose loss is smaller.
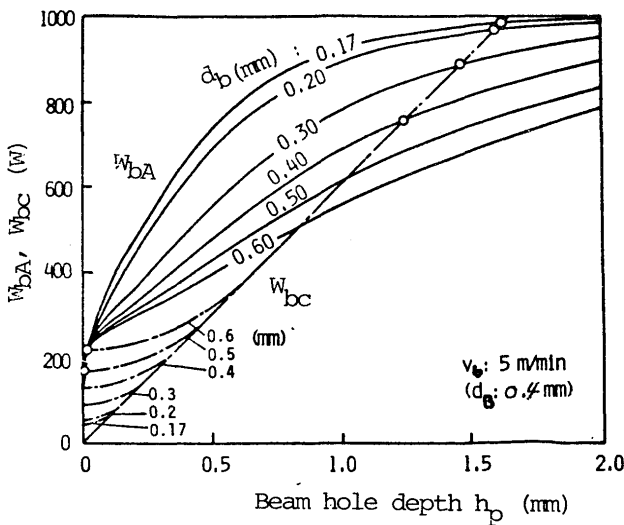

Fig. 21 Relation between h_p and W_{bA}, W_{bC}.

3.2. Penetrated heat sources

In many cases, so far analysis on physical properties of

the weld zone was based on thermal conduction theory, the "Point" or "Line" heat source theory. However, these theories were not sufficient for establishing the characteristic properties of high energy density beam heat processing. Therefore, the author proposed following two new theories: The "$\alpha\beta$-Distributed Heat Source[44]" and the "Band Heat Source[45]".

3.2.1. $\alpha\beta$-distributed heat source

Figure 22 shows various types of heat sources. The $\alpha\beta$-distributed heat source is a generalized type of heat source, (Fig. 22 (c)), which includes the point (Fig. 22 (a)) and line heat sources (Fig. 22(b)) as its special cases.

The dimensionless input energy $Q^*(\beta)$ is expressed as follows:
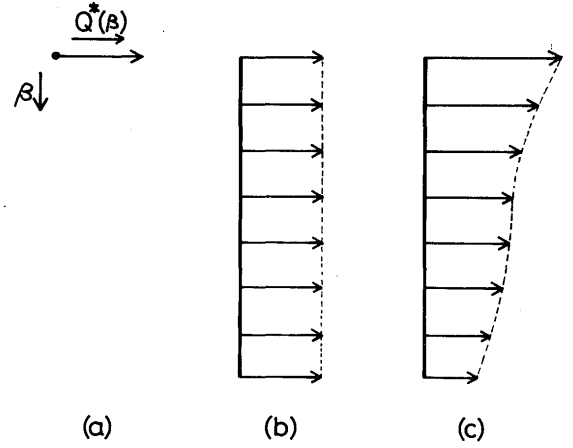

Fig. 22 Various types of heat source.

$$Q^*(\beta) = (1-\beta)^\alpha \tag{8}$$

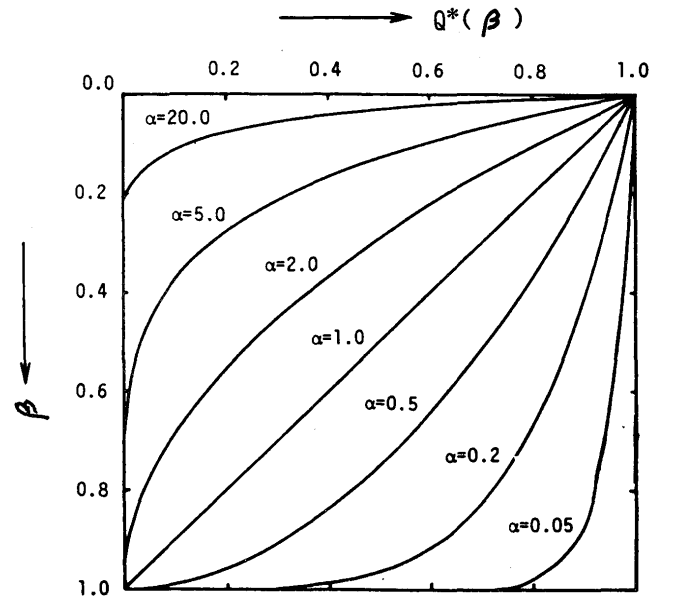where β is a dimensionless distance and α is the index to

Fig. 23 Input energy distribution function $Q^*(\beta)$.

the input energy distribution.

When $\alpha = 0$,

$$Q^*(\beta) = 1 \tag{9}$$

and it corresponds to a line heat source of uniform input energy distribution.

When $\alpha = \infty$

$$Q^*(\beta) = 1 \quad (\beta = 0)$$
$$= 0 \quad (\beta \neq 0) \tag{10}$$

and it corresponds to a point heat source. The dependence of $Q^*(\beta)$ on β is shown in **Fig. 23**.

3.2.2. Band heat source

As shown in **Fig. 24**, a rectangle is considered to be equal to the weld zone bead cross section S_B (= $\int_{-hp}^{hp} d_B(z) dz$), and $\tilde{d}_B$ is given so that $S_B = h_p \tilde{d}_B$. This is to be called the "effective bead width" as compared with the actual surface bead width d_B. This kind of rectangular heat source can be made similar to a band heat source if $h_p \gg \tilde{d}_B$ within an infinite solid body. We obtain the following formula[46]:
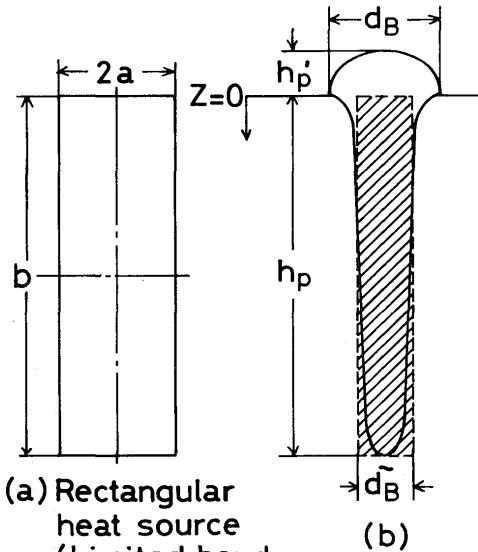

(a) Rectangular heat source (Limited band heat source)

(b)

Fig. 24 Relation between rectangular heat source and actual weld bead.

$$T_M^* = \frac{1}{\pi v_b^*} \left(\frac{\pi}{2} - \int_0^{\pi/2} \exp\left(-\frac{2v_b^*}{\cos\varphi}\right) d\varphi \right) \tag{a}$$

$$= \frac{1}{2v_b^*} \quad (\text{where } v_b^* \gtrless 1) \tag{b} \tag{11}$$

where T_M^* is the dimensionless quantity of melting temperature T_M, and v_b^* corresponds to the dimensionless quantity of welding speed v_b. With κ and κ_D as the material's thermal conductivity and thermal diffusivity, respectively:

$$T_M^* = \frac{T_M}{\left(\frac{W_b}{4\kappa b}\right)} = \frac{1}{\left(\frac{W_b}{4\kappa T_M b}\right)} = \frac{1}{W_b^*} \tag{a}$$

$$= \left(\frac{4\kappa T_M}{W_b}\right) h_p \quad (\text{where } b = h_p) \tag{b} \tag{12}$$

$$v_b^* = \frac{a v_b}{2\kappa_D} \tag{c}$$

$$= \frac{v_b \tilde{d}_B}{4\kappa_D} \quad (\text{where } 2a = \tilde{d}_B) \tag{d} \tag{13}$$

From formulae (10)(b), (11)(b) and (12)(b), the penetration depth can theoretically be induced as

$$h_p = 0.5 \left(\frac{W_b}{\kappa T_M}\right) \left(\frac{\kappa_D}{v_b \tilde{d}_B}\right) \tag{14}$$

where, however, it is assumed that 100% of the beam power W_b is absorbed into the material, and such problems as slight differences between actual bead shape and rectangular bead shape, actual molten pool temperature, beam hole formation and vapor pressure in the beam hole, etc. are ignored, in order to process purely by the theory of heat conduction alone. For that reason, with the parameters kept unchanged, the theoretical formula (14) can be written as the following empirical formula:

$$h_p = K \left(\frac{W_b}{\kappa T_M}\right)^n \left(\frac{\kappa_D}{v_b \tilde{d}_B}\right)^m \tag{15}$$

where K, n and m are experimental constants. As shown in **Fig. 25**, if K = 0.35, n = 1 and m = 0.83, you can see
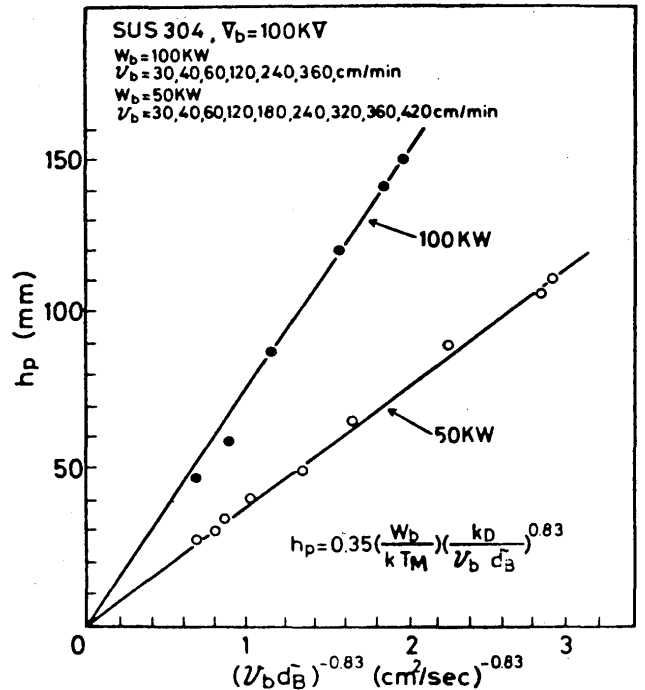

Fig. 25 Relation between h_p and $(v_b \tilde{d}_B)^{-0.83}$.

how the calculated value according to formula (15) meets the value of the actual measurement.

However, in other tests, there are cases where one parameter is chosen to express an experimental formula such as $h_p \propto 1/\sqrt{v_b}$ or $h_p \propto W_b^{1.7}$ for example. This means that compared with formula (15), there seems to be a considerable difference in the extent of the factors' contributions. That is because the phenomenon of penetration is affected by many closely interrelated factors. Their degree of contribution appears different due merely to the selection of a specific factor as a parameter or constant to simplify the relative formulae. Also, care should be taken as to the applicable limits of the formulae if only one parameter is chosen to make an experimental formula. When formulae (14) and (15) are compared, no great difference is found between the theoretical formula and the experimental one except that the K-value changes from 0.5 to 0.35 and the m-value from 1 to 0.83. These differences are considered to have been caused by the combination of the various conditions mentioned just after formula (14), but it can be seen that their effects are not so conspicuous.

Formulae (14) and (15) may further be changed and rewritten as formulae (16) and (17) as follows:
From formulae (11)(b) and (12)(a), the relation between speed and the incoming heat of a dimensionless quantity can be found by:

$$v_b^* = 0.5W_b^* \quad \text{(provided that } v_b^* \gtrsim 1) \qquad (16)$$

This is nothing but formula (14), and W_b^* is the dimen-

sionless quantity of incoming heat W_b. An experimental formula corresponding to formula (16) is then set up:

$$v_b^* = K_1 W_b^{*\ell} \qquad (17)\,(a)$$

And if the experimental parameters of formula (15) (K = 0.35, n = 1, m = 0.83) are employed, we get $K_1 = 0.375$ and $\ell = 1.2$ from the above formula, giving us:

$$v_b^* = 0.375W_b^{*1.2} \qquad (17)\,(b)$$

As shown in **Fig. 26**, formulae (16) and (17)(b) conform well in a very wide range to the linear equation

$$v_b^* = 0.59W_b^* - 0.34 \qquad (18)$$

which was found by the method of least squares, based not only on the actual measurements obtained by the
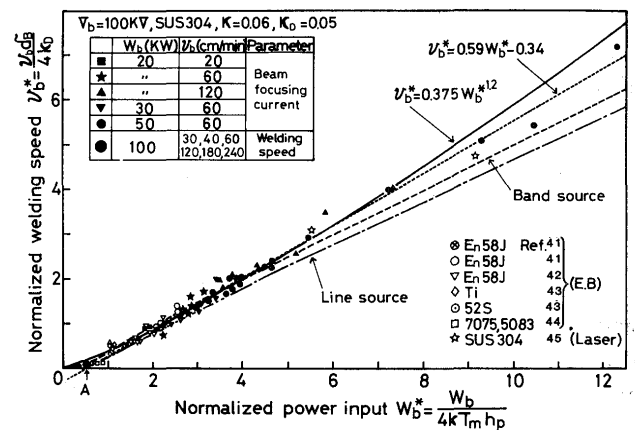

Fig. 26 Comparison of the experimental values with calculated values on v_b^* and W_b^*.

Table 1 Experimental conditions of other researchers.

Reference	41	42	43		44	45
Material	En58J	En58J	52S	Ti	7075	5083	SUS 304
K(cal/cm.sec.°C)	0.07	0.07	0.4	0.065	0.31	0.28	0.06
K_D(cm²/sec)	0.05	0.05	0.76	0.08	0.48	0.46	0.05
Beam	Electron Beam						Laser
	130KV 40mA	27–33KV,150mA	30KV, 100mA	150KV, 30mA	150KV, 7mA		20KW
v_b(cm/min)	120–300	66	66	50	150		126–430
Parameter	Welding speed	Beam focusing current	Focusing current and focus Position	Work distance			Welding speed

Table 2 Chemical compositions of materials used. W_t(%)◄─┼─►PPm

	C	Si	Mn	Cu	Ni	Cr	Al	Mg	Mo	Ti	Zn	Fe	P	S	N	O
En58J	0.06	—	—	—	10.89	—	17.65	—	2.85	—	—	Re	—	—	—	—
52S	—	0.1	—	0.04	—	0.17	Re	2.4	—	—	—	0.18	—	—	—	—
7075	—	0.11	0.03	1.6	—	0.22	Re	2.4	—	—	5.56	0.27	—	—	—	—
5083	—	<0.4	0.3–0.1	<0.1	—	—	Re	38~48	—	<0.2	<0.1	<0.4	—	—	—	—
SUS 304	0.05	0.74	1.74	0.12	10.9	19.5	0.015	—	0.16	—	—	Re	0.030	0.010	365	70
SM 41	0.18	0.47	0.71	—	—	—	0.050	—	—	—	—	Re	0.015	0.010	68	36

Re:remainder

author (shown in black symbols), but also on many actual measurements obtained by other researchers[47]−[51] (indicated in white symbols). **Table 1** shows the experimental conditions and **Table 2** the chemical compositions of the materials used. Formula (18) is found in a wide range of W_b^*, from low power to 100 kW class. However, in a low power range, $v_b^* = 0$ is obtained at $W_b^* \approx 0.57$ (point A on the horizontal axis in **Fig. 26**). Hence it is obvious that any value below this value is inapplicable. In the case of electron beam welding, the applicable range of the most popular conventional line heat source is, as seen from **Fig. 26**, $W_b^* \approx 1 \sim 4$ at most, so both the theoretical and experimental formulae based on the band heat source agree well with the linear formula obtained by using the method of least squares on a fairly wide range of actual measurements.

It seems that the melting efficiency of electron beam welding has not been fully clarified. The melting efficiency may be defined as follows:

$$\eta_M = \frac{\text{Quantity of heat required to raise the temperature of bead area to the melting temperature (cal/sec)}}{\text{Input heat to base metal (cal/sec)}}$$

$$= \frac{h_p \tilde{d}_B v_b (\rho C T_M + Q_L)}{\eta_b W_b} \qquad (19)$$

where, ρ, C and Q_L are density of the base metal, specific heat and latent heat, respectively, and the other symbols are all those already mentioned. If the beam's melting

efficiency of the base metal is represented by η_b and $Q_L \to 0$, $\eta_b \to 1$, then formula (19) becomes

$$\eta_M = \frac{v_b^*}{W_b^*} \times 100 \ (\%) \qquad (20)$$

where if theoretical formula (16) is employed, $\eta_M = 50\%$ is obtained. This is inexplicable because normally about 60% is obtained in actual measurements as shown in **Fig. 27**. Actually, however, $Q_L = 0$ and the molten pool temperature is greater than T_M, so from formula (19), it is obvious that $\eta_M > 50\%$. Thus it may be quantitatively expressed using formula (18).

$$\eta_M = \frac{0.59}{1 + \frac{0.34}{v_b^*}} \qquad (21)$$

From this we can get $\eta_M \lesssim 60\%$ and see that it almost fully conforms to the actual measurement. Even in this case, a line heat source can be used only in a narrow range where the value of v_b^* is not more than 1.5 or so.

3.3 Surface heat source

Here we describe the characteristics of a "surface heat source" employed large output high energy density beams by which the material surface is not or only slightly melted.

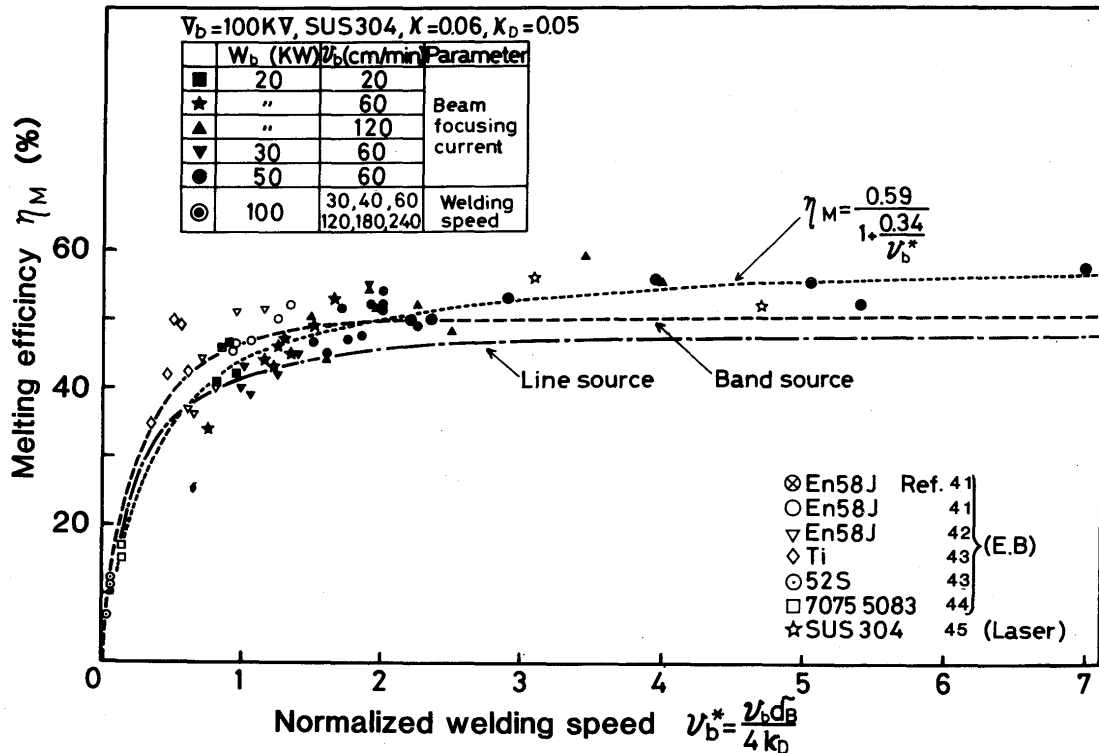This applied mainly to such processes as quenching and

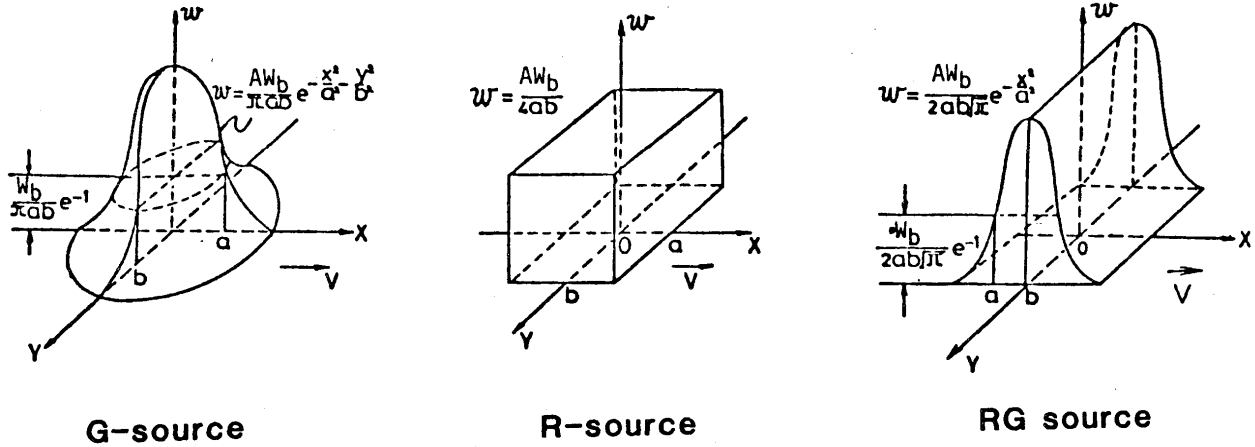Fig. 27 Comparison of experimental melting efficiency and calculated ones.

G-source   **R-source**   **RG source**

Fig. 28 Intensity distribution of surface heat source.

other surface treatments, surface alloying and so on. In most cases, as shown in **Fig. 28**, the temperature distribution of surface heat sources can be considered to have three types: a Gaussian distribution (its cross section is generally elliptical, but in special cases circular; G-heat source), a rectangular distribution (uniform temperature; R-heat source), and a rectangular-Gaussian distribution (the above two types are overlapped; RG-heat source)[52]. Such a heat source distribution can be obtained by properly modifying the multiple mode of the beam, by using a special optical system with a segment mirror, or by using a beam oscillator.

As mentioned earlier, the beam's reflection loss against metal is small in the case of an electron beam, but extremely great in the case of a laser. For example, with a CO_2 laser, even on a molten surface with the highest absorptivity, you can only achieve $A_b \approx 15\%$ at best. Thus, to quench steel material with low output CO_2 lasers, we tried to increase A_b by lightly coating the surface with a phosphite film for example. This enabled us to attain $A_b = 50$ to 90% under conditions where the surface was not melted, as shown in **Fig. 29**. In this case, the
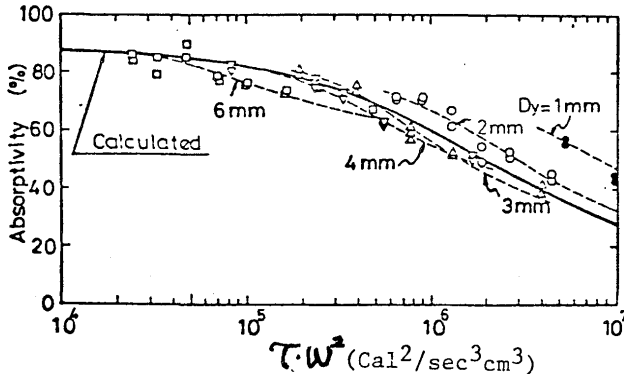

Fig. 29 Absorptivity plotted as a function of τw^2 (τ = interaction time, w = power density). The absorptivity can be predicted from this figure independently of beam spot shape, laser power and travelling velocity.

important parameter is τw^2 where the laser strength is $w(r)$ and its dwell time τ. Thus we can find the A_b value of the surface irrespective of the beam spot, beam output and beam travelling speed. Under such surface condition, if scanned by large output high density beams, the surface is rapidly heated and its heat affected zone appears only in the vicinity of the surface. Thus, in this case, the temperature distribution in the stationary state can be obtained from the following formula (dimensionlessly displayed) providing that the said distributed heat source travels on a semi-infinite plate at a speed of v_b.

$$T_G^* = \frac{16}{\pi} \int_0^\infty \frac{1}{\sqrt{(a^{*2}+t^{*2})(b^{*2}+t^{*2})}}$$
$$\times \exp[-\frac{(2x^*+v^*t^{*2})^2}{4(a^{*2}+t^{*2})} - \frac{y^{*2}}{b^{*2}+t^{*2}} - \frac{z^{*2}}{t^{*2}}]dt^*$$
(G-source) $\cdots\cdots$ (22)

$$T_R^* = \int_0^\infty (\mathrm{erf}\,\frac{2x^*+v^*t^{*2}+2a^*}{2t^*} - \mathrm{erf}\,\frac{2x^*+v^*t^{*2}-2a^*}{2t^*})$$
$$\times (\mathrm{erf}\,\frac{y^*+b^*}{t^*} - \mathrm{erf}\,\frac{y^*-b^*}{t^*})\exp(-\frac{z^{*2}}{t^{*2}})\,dt^*$$
(R-source) $\cdots\cdots$ (23)

$$T_{RG}^* = \frac{4}{\sqrt{\pi}}\int_0^\infty \frac{1}{\sqrt{a^{*2}+t^{*2}}}\exp[-\frac{(2x^*+v^{*2})^2}{4(a^{*2}+t^{*2})} - \frac{z^{*2}}{t^{*2}}]$$
$$\times (\mathrm{erf}\,\frac{y^*+b^*}{t^*} - \mathrm{erf}\,\frac{y^*-b^*}{t^*})\frac{dt^*}{b^*}$$
(RG-source) $\cdots\cdots$ (24)

providing that $T^* = 16\sqrt{\pi}\,\kappa rT/A_bW_b$, $v_b^* = rv_b/2\kappa_D$,

$x^* = \frac{x}{r}$, $y^* = \frac{y}{r}$, $z^* = \frac{z}{r}$, $a^* = \frac{a}{r}$, $b^* = \frac{b}{r}$, $r^2 = ab$

and $\mathrm{erf}\xi = \frac{2}{\sqrt{\pi}}\int_0^\xi \exp(-u^2)du$ with κ = thermal conductivity, κ_D = thermal diffusivity, T = temperature, W_b = laser power, A_b = beam absorptivity and v_b = travell-
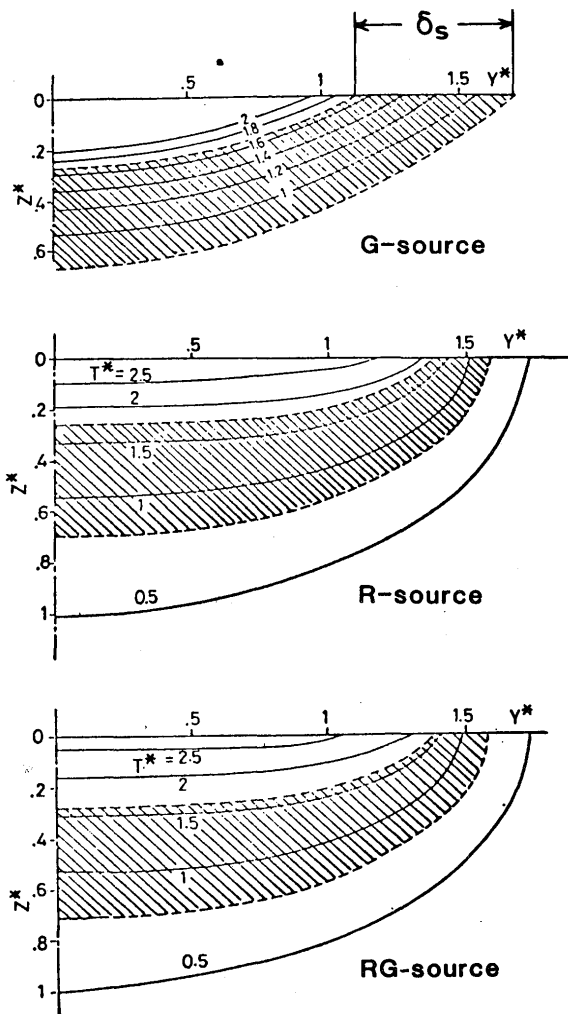
Fig. 30 Isothermal lines ($v_b^* = 4$). The hatched region corresponds to the softened zone. The value of T in this region varies from $(4/15)T_{max}^*$ and $(8.5/15)$ T_{max}^*. T_{max}^* is defined to be the temperature at the origin (Z = 0, Y = 0).

ing speed.

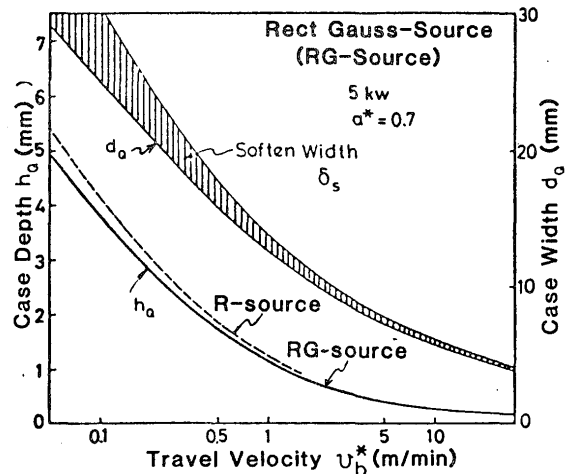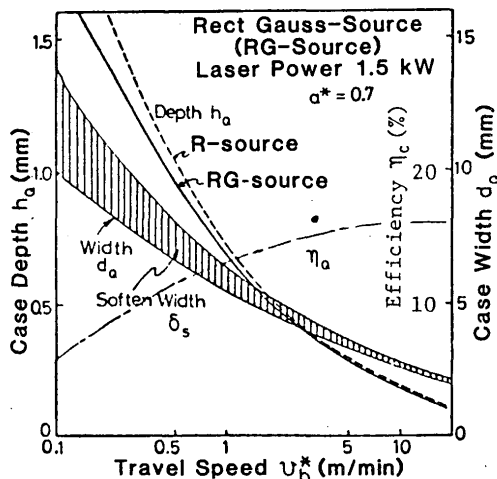**Figure 30** shows the isothermal lines drawn using the

above formulae (22) to (24) for each heat source. The hatched area in the figure shows the cross sectional configuration of the temperature range from $\frac{4}{15} T_{max}^*$ to $\frac{8.5}{15} T_{max}^*$ and corresponds to the softening zone affected by heat. The magnitude of the width of this softening zone, "softening width" δ_s, on the metal surface is important from a practical viewpoint. This indicates that a G-source is not practical because it enlarges the softening width, whereas R- and RG-sources are more useful because their softening widths are narrower.

Figure 31 shows the maximum hardening depth (hardening temperature: 850°C, surface temperature: 1500°C and a* = 0.7) in the case of RG-source. This is an example calculated with beam output W_b = 1.5 kW and W_b = 5 kW. To find out the extent of the effect according to the type of heat source, the result for R-source is also shown. This indicates that there is no great difference between R and RG heat sources.

In the same figure we also plotted the softening width δ_s when steel is quenched by a laser. The quenching efficiency η_Q is the ratio of the thermal capacity required (when the softened zone of the metal is adiabatically heated to 850°C) to that of the input laser. η_Q increases proportionally to v_b^* as shown in **Fig. 31**.

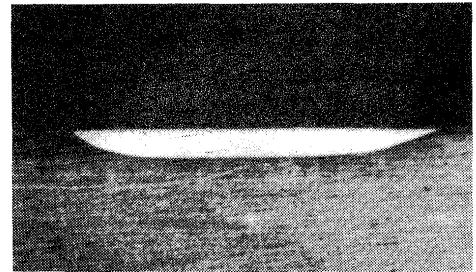**Figure 32** shows the hardened zone of tool steel SK-5 quenched by a 1 kW laser of RG distribution, and **Fig. 33**

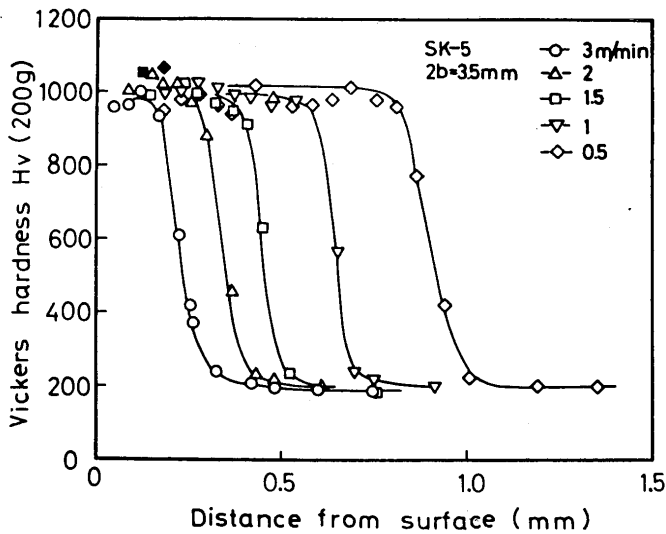**Fig. 32** Cross section of laser hardened SK-5 (Case depth = 0.25 mm).

Fig. 31 Hardened depth h_c, hardened width d_c and softened with δ_s for two laser powers as RG-source.

Fig. 33 Hardness distribution of SK-5.

Fig. 35 Relation between heated temperature and hardness.

shows the hardness distribution in this case. This hardness is about $H_v = 100$ higher than in the case of water quenching, which indicates that it is difficult for austenite to remain. In this case, the cooling time $\tau_{800 \to 400}$(sec) is considerably short as shown in Fig. 34. In normal quenching, as further shown in Fig. 35, there is a relationship between the temperature at which the maximum hardness T_{Hm} is attained and the temperature at which to start hardening T_{Hs} (determinated by C%). As shown in Fig. 36, T_{Hm} is usually considerably higher than the A_{c3} transformation. Up to about 0.4%C it rapidly drops from 1200°C to 900°C as the amount of carbon increases. After that, even if the amount of carbon increases, it stays constant at 900°C or so. T_{Hs} is not so affected by the amount of carbon and stays constant at about 750°C.
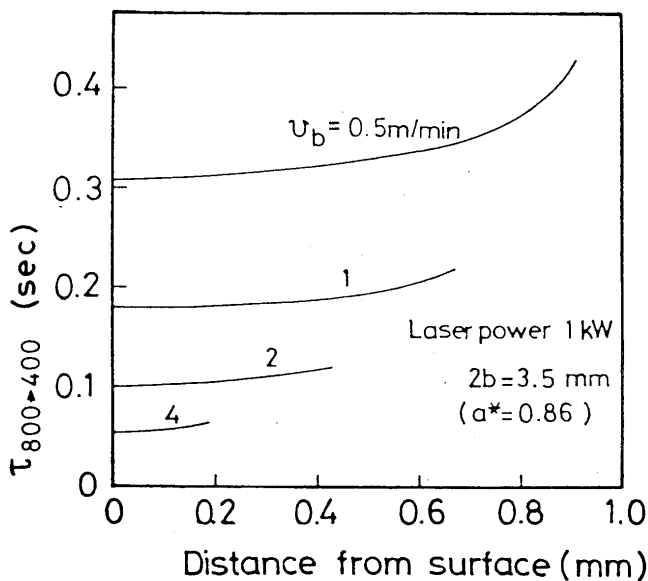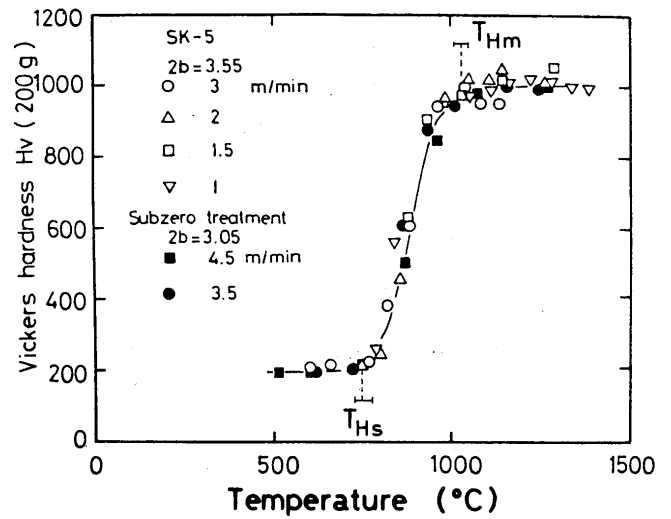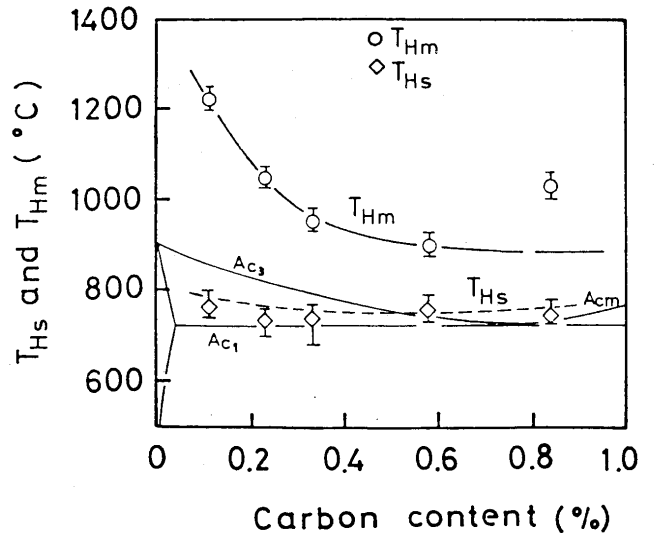

Fig. 36 Effect of C% on T_{Hm} and T_{Hs}.

4. Basic Physical Characteristics of the Ultra High Energy Density Beam Weld Zone

A weld zone by high energy density beam has a specially peculiar shape in the bead cross section with narrow band. Moreover rapid heating and cooling processes are dominant in this zone during welding. These features inherently give rise to also peculiar physical properties of the weld. Here we describe about hardness and some mechanical properties.

4.1. Hardness

We have examined the hardness of the weld in about 100 kinds of steel. Generally speaking, the hardness is the function of both the element term f (E) and cooling term

Fig. 34 Cooling time from 800°C to 400°C ($\tau_{800 \to 400}$).

$$H_V = F\{ f(\tau), f(E)\} + F_o, \quad \text{- - - - - [A]}$$

$$H_V = F\{ f(\tau_{T_1 \to T_2}), C_{eq}\} + B, \quad \text{- - - - - (1)}$$

$$F = \frac{A}{\tau_{T_1 \to T_2}^K} C_{eq'}, \quad \text{- - - - - (2)}$$

$$H_V = \left\{ \frac{840}{\tau_{800 \to 500}^{0.22}} - C_{eq} + 58 \right\} \pm 66, \quad \text{- - - - - (3)}$$

$$[C_{eq}] = [C] + \frac{[Mn]}{2.4} + \frac{[Si]}{24} + \frac{[Ni]}{14} + \frac{[Cr]}{16} + \frac{[Mo]}{60},$$

$$\tau_{800 \to 500} \stackrel{.}{=} 3.8 \times 10^{-2} \left[\frac{0.81_b V_b}{V_b h_p} \right] \left[\frac{1}{(500-T_o)^2} - \frac{1}{(800-T_o)^2} \right].$$

Fig. 37 Arata electron beam weldability.

f (τ) as expressed in equation (A) of **Fig. 37**. However, conventional hardness equations ever proposed have been based on the element term only by using carbon equivalent and the term f (τ) was completely neglected. So, we developed[53] the hardness prediction equation which includes both terms, as shown in equation (3) of **Fig. 37**. This relation was named as "Arata Electron Beam Weldability"[54]. **Figure 38** shows that the predicted hardness
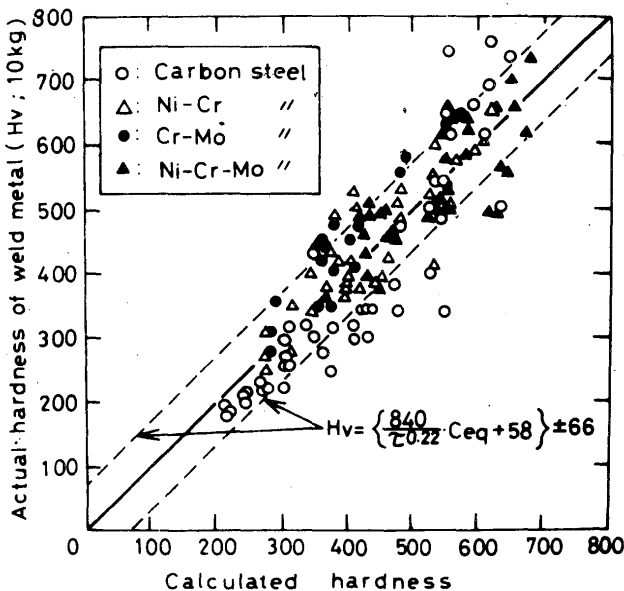

Fig. 38 Comparison of actual hardness with calculated hardness.

by this equation lies within a deviation of 66 for data published on EB welds of various types of steels conducted at a number of different research laboratories. We further developed the new hardness prediction equation by regression analysis, in order to increase the accuracy and to be applicable not only to EB and laser welds but also to arc welds[55].

Figure 39 shows the basic concept of introducing the hardness prediction equation. As is well known, the hardness changes with the cooling rate, as the curve shown in the figure shows. This characteristic curve has a close correlation with the amount of Martensite structure. Points A and B represent the points where the amount of Martensite is 100% and 0%, respectively, in the microstructure. The cooling rate and hardness at each point are formulated by regression analysis as shown at the bottom of the figure and thus the hardness at an arbitrary cooling rate is expressed by the equation in the rectangular box. In **Fig. 40** the accuracy of several hardness equations[56], [57] is compared for the same data for many kinds of steel. It is clear that the new Arata's equation can predict the hardness with much higher accuracy.
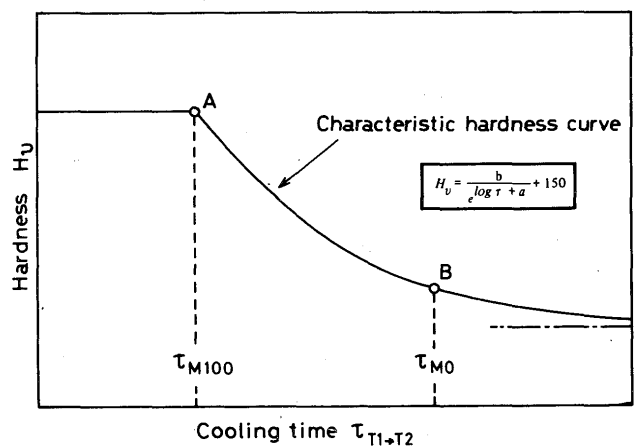
A: $H_v(\tau_{M100}) = 835[C] + 287$, $\log \tau_{M100} = 2.55([C] + \frac{1}{6.3}[Mn] + \frac{1}{3.6}[Si]) - 0.92$.

B: $H_v(\tau_{M0}) = 273([C] + \frac{1}{13}[Mn] + \frac{1}{9.7}[Si]) + 133$,

$\log \tau_{M0} = -0.37([C] - \frac{1}{1.1}[Mn] - \frac{1}{0.44}[Si]) + 1.02$.

Fig. 39 Relation between cooling time and hardness.

4.2. Fracture path transition temperature: $_ITF$

The other problem of mechanical properties that is inherently caused by the narrow bead shape is the problem of "Fracture Path Transition Temperature, $_ITF$"[58] Figure 41 shows some examples of Charpy, deep notch and COD test. In every test, the behavior of the fracture path is almost the same and is dependent on the temperature. This is a significant problem, particularly when we evaluate the impact test values.

In order to evaluate the change in fracture path quantitatively, we have defined the following parameters as shown in Fig. 42. δH_v is the relative hardness difference between the weld and mother plate, and F_p is the fracture path parameter which represents the shape factor of the
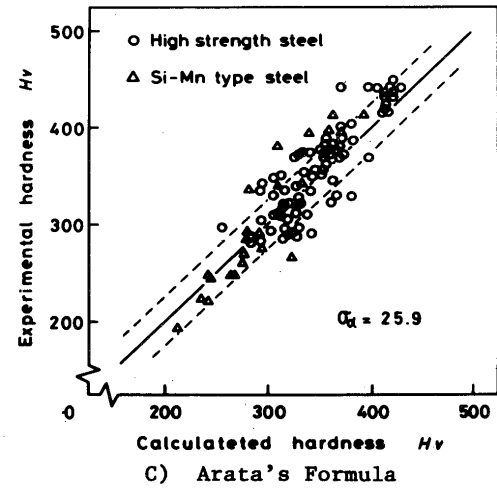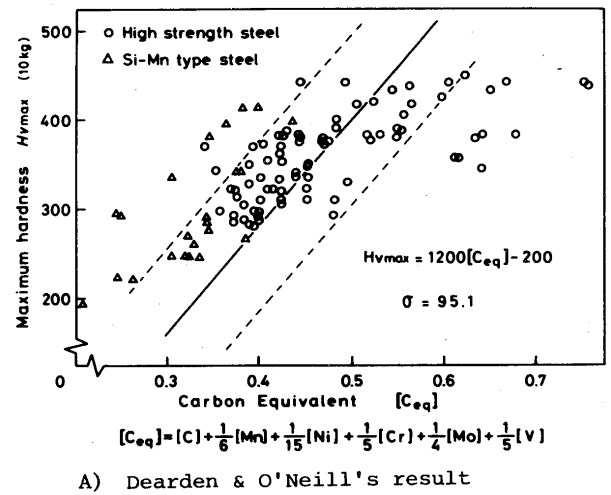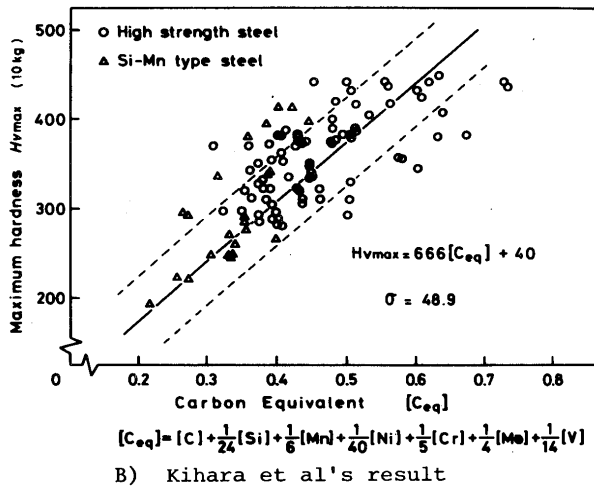
A graph with axes: x-axis "Carbon Equivalent [C_{eq}]" from 0.3 to 0.7, y-axis "Maximum hardness $Hvmax$ (10 kg)" from 0 to 500. Legend: o High strength steel, Δ Si-Mn type steel.

$Hvmax = 1200[C_{eq}] - 200$

$\sigma = 95.1$

$[C_{eq}] = [C] + \frac{1}{6}[Mn] + \frac{1}{15}[Ni] + \frac{1}{5}[Cr] + \frac{1}{4}[Mo] + \frac{1}{5}[V]$

A) Dearden & O'Neill's result

A graph with axes: x-axis "Carbon Equivalent [C_{eq}]" from 0.2 to 0.8, y-axis "Maximum hardness $Hvmax$ (10 kg)" from 0 to 500. Legend: o High strength steel, Δ Si-Mn type steel.

$Hvmax = 666[C_{eq}] + 40$

$\sigma = 48.9$

$[C_{eq}] = [C] + \frac{1}{24}[Si] + \frac{1}{6}[Mn] + \frac{1}{40}[Ni] + \frac{1}{5}[Cr] + \frac{1}{4}[Mo] + \frac{1}{14}[V]$

B) Kihara et al's result

A graph with axes: x-axis "Calculateted hardness Hv" from 200 to 500, y-axis "Experimental hardness Hv" from 0 to 500. Legend: o High strength steel, Δ Si-Mn type steel.

$\sigma_d = 25.9$

C) Arata's Formula

Fig. 40 Comparison between traditional equations and Arata's formula.
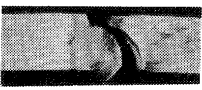
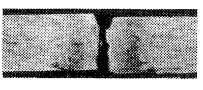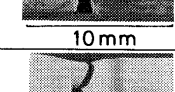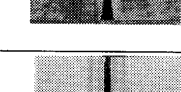| Heat input 10 kJ/cm	Testing temperature	
	0°C	-60°C
Charpy test (HT50)	10 mm	
COD test (HT50)	10 mm	
Deep notch test (HT80)	10 mm	

Fig. 41 Some examples of COD, deep notch and charpy tests.

Hardness of weld metal; $H_{v,w}$

Hardness of base metal; $H_{v,B}$

Hardenability

$\delta H_v \left(\frac{H_{v,w} - H_{v,B}}{H_{v,B}} \right)$

V-notch

HAZ

Fractured in ; Weld metal Base metal

Fracture expectation zone; $(d_B \times h)$
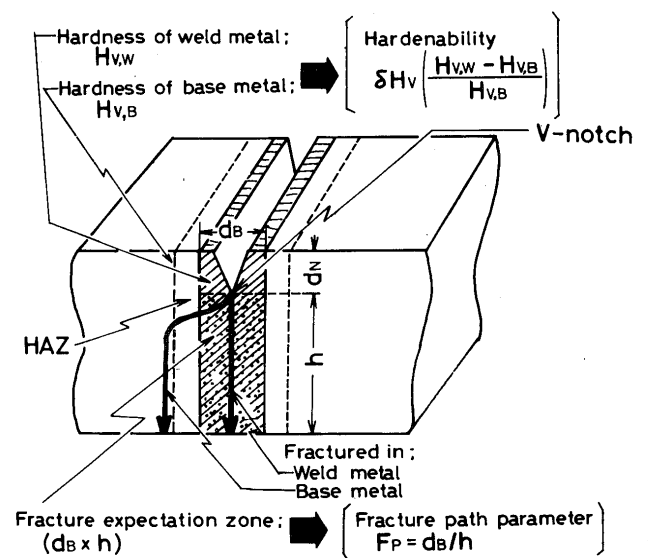
Fracture path parameter $F_P = d_B / h$

Fig. 42 Schematic illustration for two types of fracture path observed in charpy test etc.
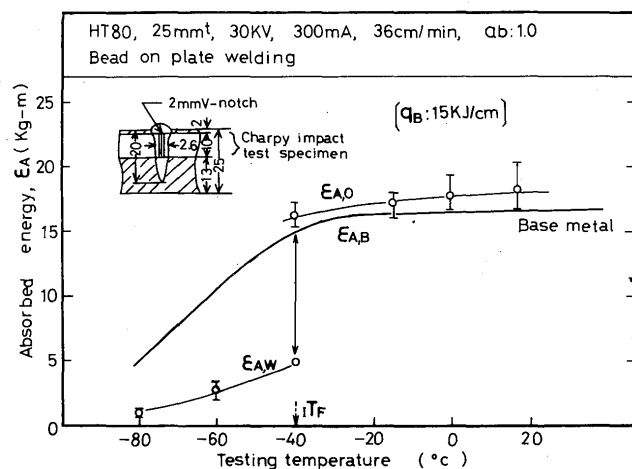
Fig. 43 Transition temperature curve.

bead. **Figure 43** shows an example of impact test, in which one can clearly see the existence of fracture path transition temperature $_IT_F$ when Charpy test is conducted on a welded joint. ϵ_{AO} shows when fracture path turns aside from the weld to the base metal, and ϵ_{AW} shows when the path remains in the weld metal. This figure also includes the test results of the base metal shown by curve ϵ_{AB}. In this way, the impact value for EB welded joint differs considerably depending on the fracture path. It is, therefore, very important to consider this phenomenon when one examines the impact values for the welded joint. While **Fig. 44** shows an example how the transition
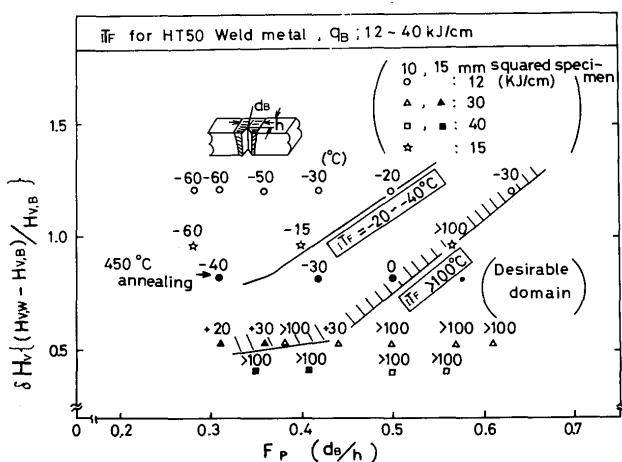
Fig. 44 Settlement for $_IT_F$ by using δH_V and F_p parameters.

temperature changes also with the difference in hardness and the fracture path parameter. These parameters are a function of the welding conditions and material, so one has to choose the optimum conditions using this kind of diagram. In the case of laser welding, similar results are obtained.

5. Application of Ultra High Energy Density Beams

5.1. Electron beam welding

5.1.1. Horizontal electron beam welding

In electron beam welding, it is essential that the electron gun should operate efficiently, and since the gun is considerably heavy and a high degree of accuracy is required, it must in general be fixed in position or supported by a machine as a robot. Therefore, it was said to be too difficult to perform electron beam welding in a variety of positions. It has been made possible by developing a beam deflector[59], as shown in **Fig. 45**. Figure 45 shows both
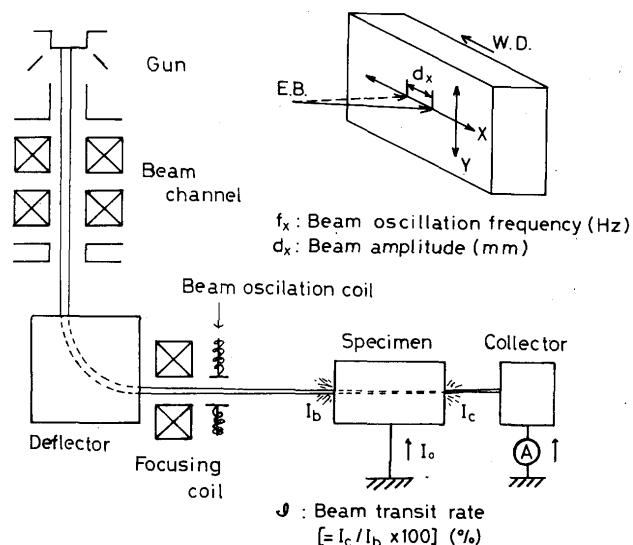

Fig. 45 Schematic diagram of beam oscillation at horizontal beam.

the experimental method and conditions. Namely, we used the 90° deflected horizontal beam. Some important beam parameters are explained here. We defined the welding direction as the X axis and the perpendicular direction as the Y axis. In general, X-oscillation is effective for materials with low heat conductivity such as steel, and Y-oscillation is good for highly conductive materials such as Aluminum. Another important parameter is the beam transit rate, which defined by I_c over I_b. The materials used in this experiment were Cr-Mo steel (2¼Cr-1Mo), stainless steel (SUS 304), high tensile strength steel (HT 50, 80), centrifugally cast steel pipe for welded structures (SMK 50) and thick plates of a thickness of 100 mm or more. In the case of these thick plates, however, a number of defects such as porosity appear if suitable beam conditions are not chosen. One means of inhibiting such phenomena is to produce beam oscillation, i.e., to cause the beam to oscillate along the transverse line of welding by applying X-oscillation, or to cause it oscillate perpendicularly through Y-oscillation by means of a suitable magnetic field, as shown in **Fig. 45**. The oscillations

are indicated by frequency f_X, f_Y (Hz) and amplitude d_X, d_Y (mm).

The oscillation which should be chosen and the question of whether a compound oscillation (circular or elliptical in shape) is suitable depends on the material. **Figure 46** shows the effect of X-oscillation (f_X) when 100
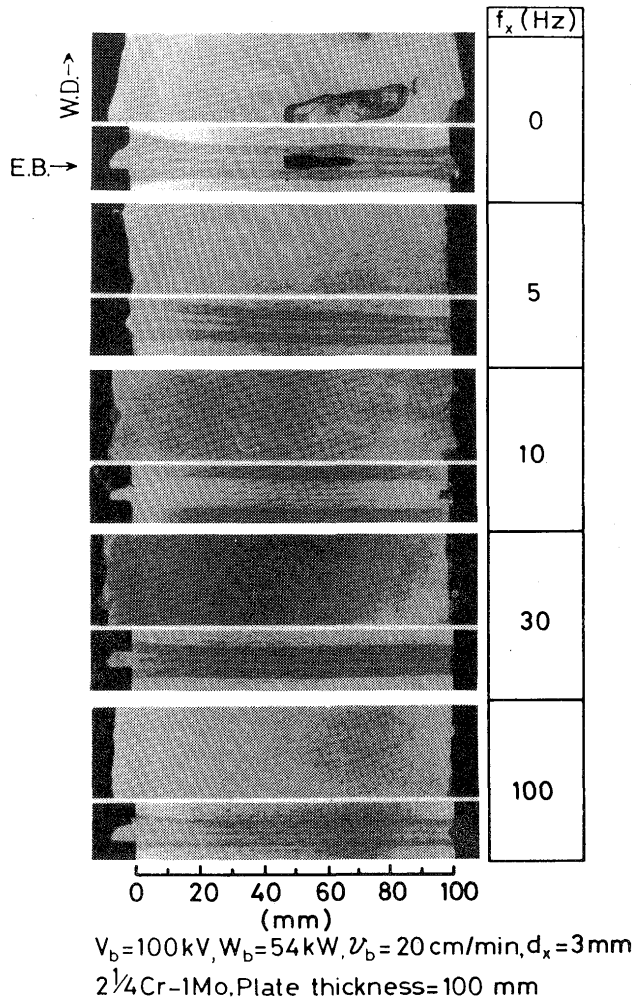

$V_b = 100\,kV, W_b = 54\,kW, \mathcal{V}_b = 20\,cm/min, d_x = 3\,mm$

$2\frac{1}{4}Cr-1Mo.Plate\ thickness = 100\ mm$

Fig. 46 Fully penetrated bead sections of horizontal position welding with various beam oscillation frequency.

Fig. 47 Relation between bead width, defect rate and beam oscillation frequency.
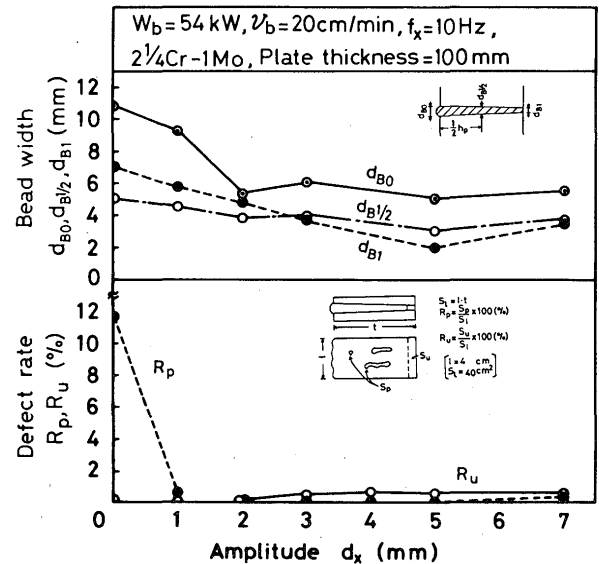
Fig. 48 Relation between bead width, defect rate and beam amplitude.

mm thick 2¼Cr-1Mo steel was welded at a welding speed of v_b = 20 cm/min[60]. **Figure 47** further illustrates these bead conditions. The results obtained are indicated by the symbols in the figure, which show the porosity rate R_p (= S/S_o) and under-fill rate R_u (= S_u/S_o). Conditions are optimum when $f_x \simeq 10$ and $d_x \simeq 2 \sim 5$. R_p and R_u being limited to almost 0. Furthermore, a condition called "parallel bead" can be obtained in the welded part, where the bead width is almost uniform throughout.

Figure 48 shows the effect of the oscillation amplitude. By selecting the optimum frequency and amplitude, it is possible to obtain a sound weld with a narrow band-shaped bead.
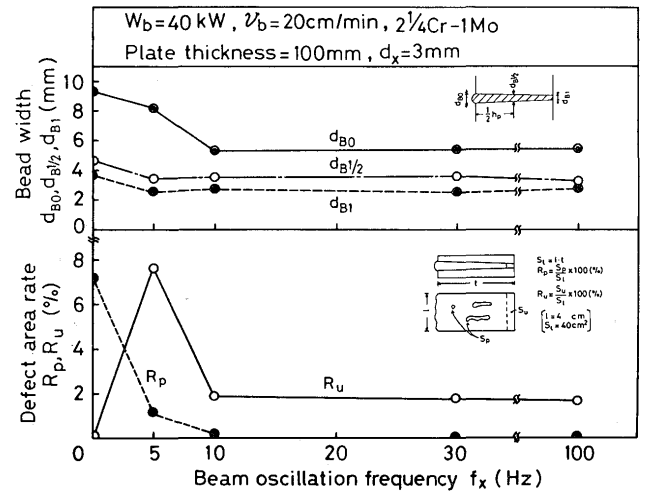
In full penetration welding, the important factor is the value of $\mathcal{J}$, the beam pass rate of the beam current. $\mathcal{J}$ = I_c/I_b : I_b indicates the incident beam current, I_c indicates the collected beam current [shown in **Fig. 45**]. The influence of the $\mathcal{J}$ values is shown in **Fig. 49**, and the range of efficiency is $\mathcal{J} \simeq 10 \sim 50$. When $\mathcal{J} \simeq 10$ and $f_x \simeq 10$, porosity completely disappeared although some under-fill still remained. When $f_x \simeq 30 \sim 100$, the under-fill also almost totally disappeared (except for $1 \sim 2\%$). The relationship of f_x, d_x and $\mathcal{J}$ is most important.

Figure 50 shows the examples of good results obtained by beam control for various kinds of steel. It is clear that the appropriate selection of beam conditions is very important to obtain a sound weld.

Figure 51 shows the influence of dissolved oxygen and nitrogen contents in steel on defect formation. As seen in
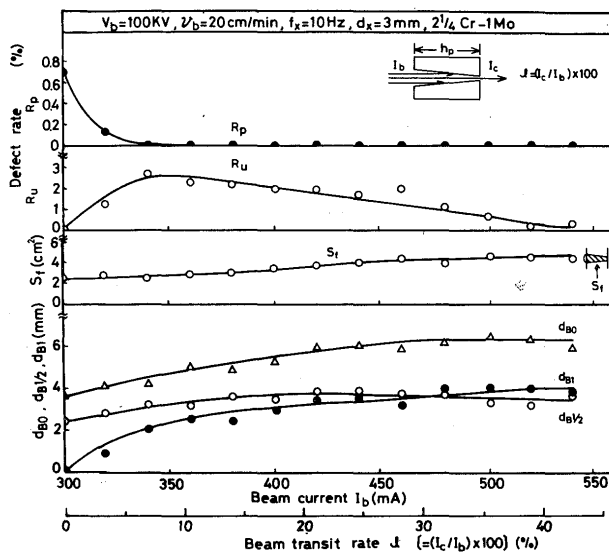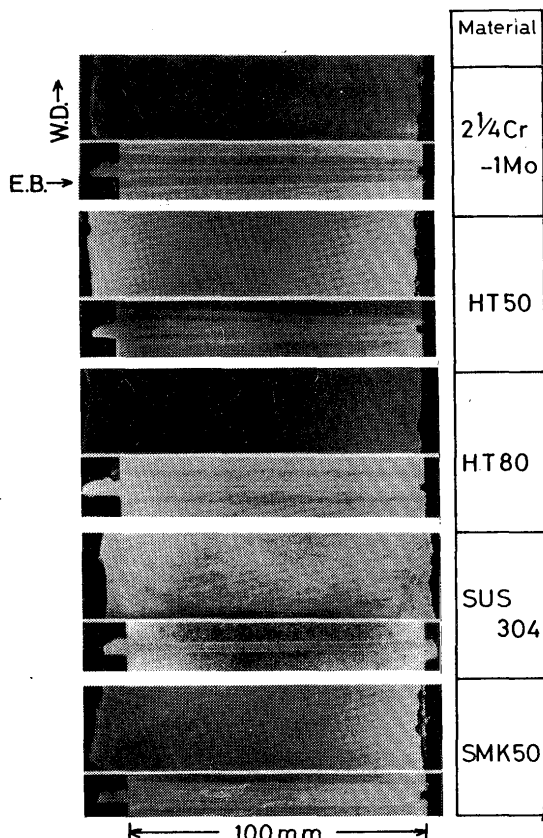
Fig. 49 Relation between bead width, defect rate and I_b, $\mathcal{J}$.

Fig. 51 Relation between defect rate and contents of [N + O].

Fig. 50 Fully penetrated bead sections of horizontal position welding with various metals.
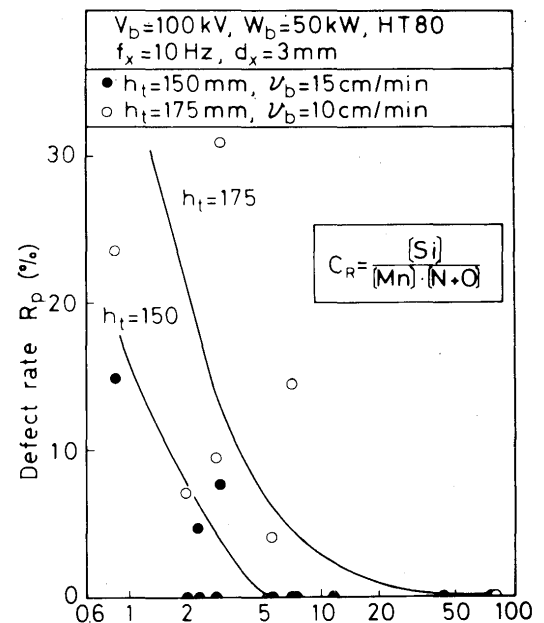
Fig. 52 Relation between defects rate and C_R.

this picture, a slight increase in plate thickness —for example, from 15 to 17.5 cm— bring about considerable effect on porosity formation. For conventional steels, the defect rate is well evaluated by the total amount of oxygen and nitrogen.
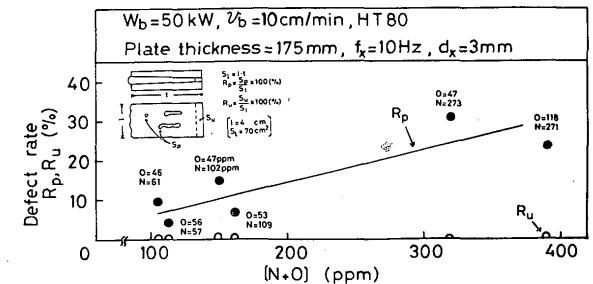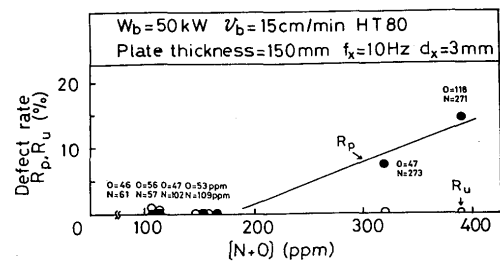
Figure 52 shows the effect of volatile elements in steel on the porosity appearance in the case of full penetration welding. In order to evaluate the contribution of these elements, we have introduced a new parameter C_R defined in the box of the figure.

In the vertical upward position welding by electron beam, the penetration depth does not saturate even at very low speed and the beam hole looks stable. It is, therefore, possible to weld very thick plates, even plates as thick as 30 cm, in this position. However, as in Fig. 53 the grain size becomes coarse as in electro-slag welding. This lowers the impact value and make it undersirable for practical use. Therefore, it is necessary to choose an opti-

Fig. 53 Fully penetrated bead cross sections of upward vertical position welding.

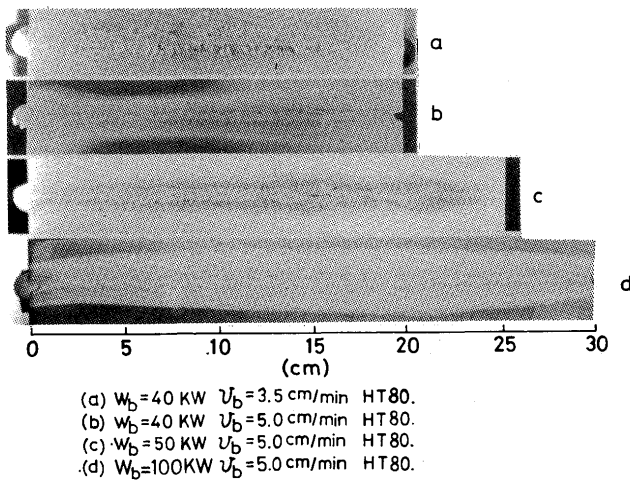(a) W_b=40 KW U_b=3.5 cm/min HT80.
(b) W_b=40 KW U_b=5.0 cm/min HT80.
(c) W_b=50 KW U_b=5.0 cm/min HT80.
(d) W_b=100KW U_b=5.0 cm/min HT80.

mum welding speed to yield the appropriate cooling rate for the material used, in order to establish the practical EB welding of 20 to 30 cm thick plate. For this sake, it became clear that a conventional 100 kW EB welder still lacks the necessary power.

Figure 54 shows[61] the example of HT 60 steel of 50 mm thickness welded by local vacuum horizontal electron beam welding. Such local vacuum EB was also applied to a vacuum chamber of SUS 304L for nuclear fusion research.

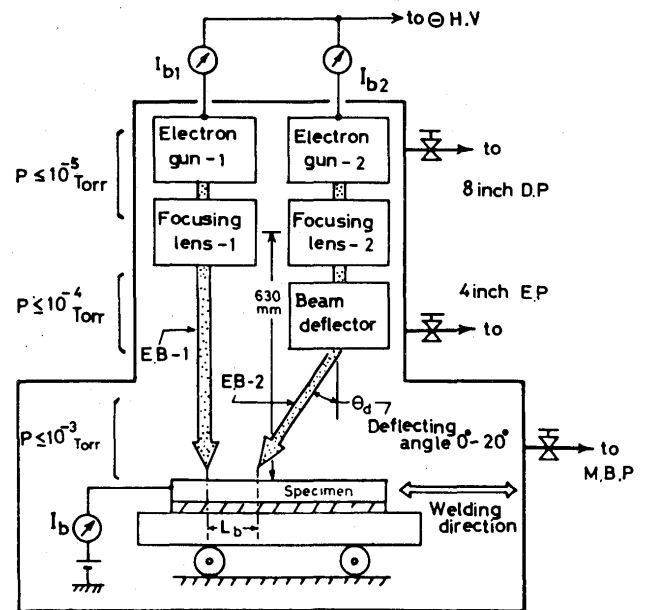Fig. 54 Appearance of welded HT 60 steel pipe (diameter 1.4 m, thickness 50 mm).

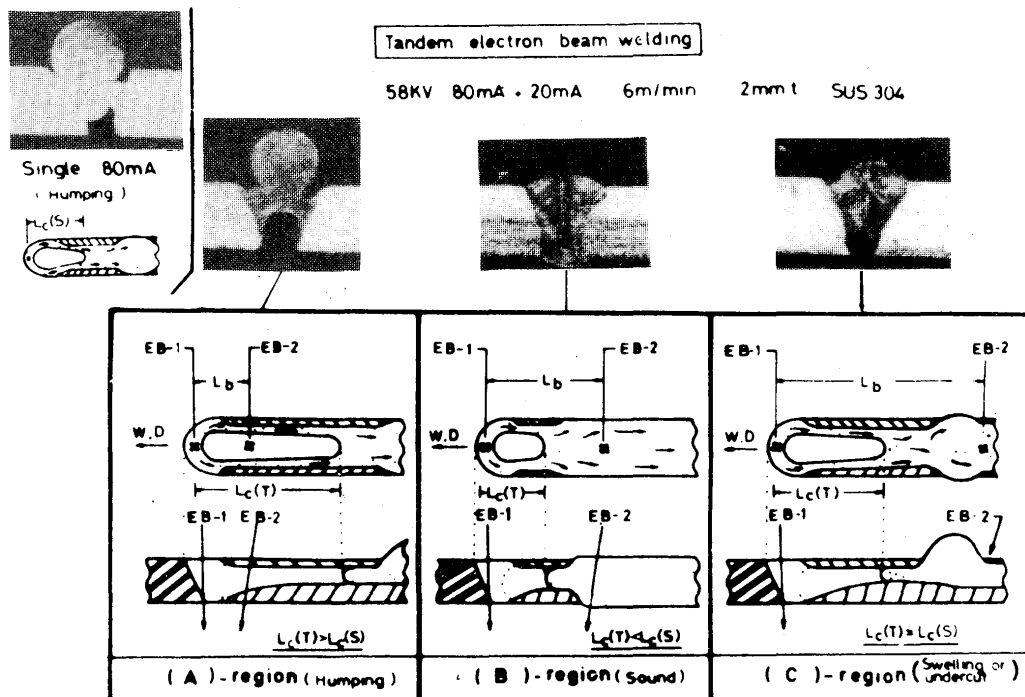Fig. 55 Schematic diagram of Tandem Electron Beam welder.

Fig. 56 Humping phenomenon and its suppression mechanism by TEB welding.

5.1.2.Tandem electron beam welding

Electron beam welding has many advantages compared with ordinary arc welding. However, it also has disadvantages caused by its high energy density, such as humping, spiking and root porosity. In order to overcome these problems, the author developed "Tandem Electron Beam Welding (TEB Welding)" as shown in **Fig. 55**[62]. This method utilizes two electron beams at the same time, one beam as a conventional single electron beam and the other as sub-beam for the repairment of welding defects.

In the case of high speed welding humping frequently occurs, as shown in **Fig. 56**. By impinging the second beam in the proper position, and separating it from the first beam by a "Tandem Gap", the humping phenomenon is suppressed as shown in **Fig. 56**. Suppression mechanism of humping is explained as shown in this figure. The second beam impinging in the proper position of molten pool changing the flow of molten metal so that it flows smoothly backward.

TEB welding can also suppress the welding defects such as spiking and root porosity which occur in deep penetration welding as shown in **Fig. 57**[63]. The suppression mechanism can be explained as follows: In the case of deep penetration welding, the second beam impinges onto the beam hole of the first beam. When the energy density of the second beam is properly low, the beam can stabilize strongly the beam hole and reheats the root zone, making any spiking and root porosity disappear. This process was revealed by high speed observa-

A·Region   B·Region   C·Region

5 mm

$W_{b2} = 3·10^4$ watt/cm^2 $W_{b2} = 6·10^4$ watt/cm^2 $W_{b2} = 6.6·10^5$ watt/cm^2

EB-1 58 Kv 80mA 9.2×10^5 W/cm^2
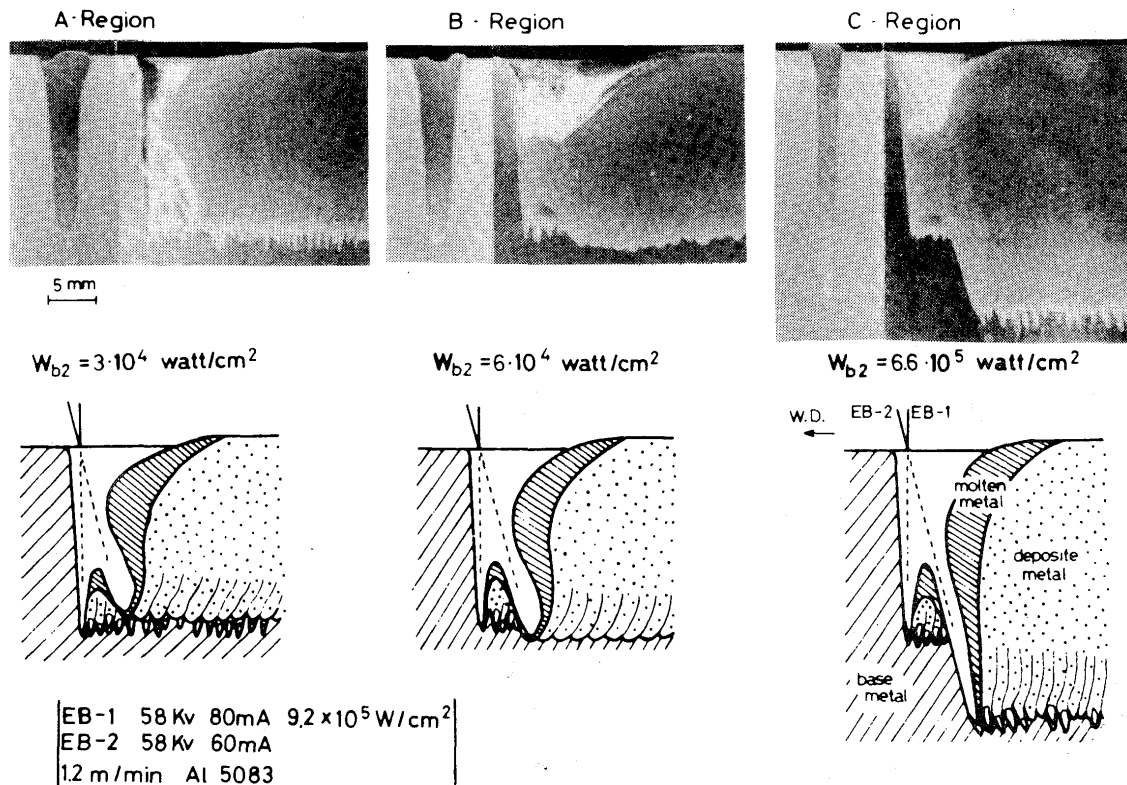EB-2 58 Kv 60mA
1.2 m/min Al 5083

Fig. 57 Spiking phenomenon and its suppression mechanism by TEB welding.
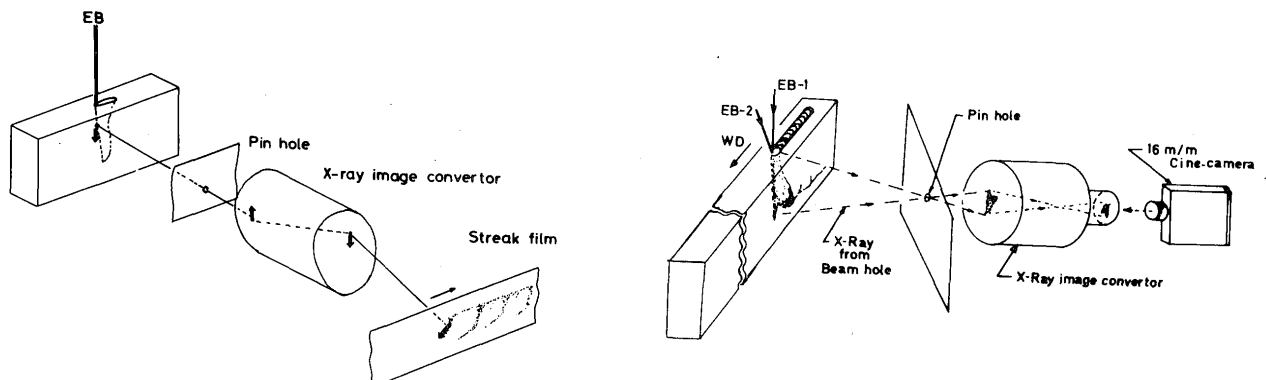

Fig. 58 High speed observation method of beam hole during welding.

tion of the beam hole X-ray[64] and transmission X-ray method[65] shown in **Fig. 58**.

The optimum power ratio between the first and second beam was determined to be 10% for aluminum alloy of 20 mm penetration[65]. For carbon steel of 30 mm penetration, it was also determined to be about 15%.

5.2. Laser welding

5.2.1.Atmospheric laser welding

Laser welding using a high power CO_2 laser can easily weld the specimen under atmospheric condition. However, in the case of atmospheric laser welding, so called "laser plasma" occurs and affects strongly the welded bead. This laser plasma can be suppressed by using inert gas as an assist gas, as shown in **Fig. 59**. The pressure of such assist
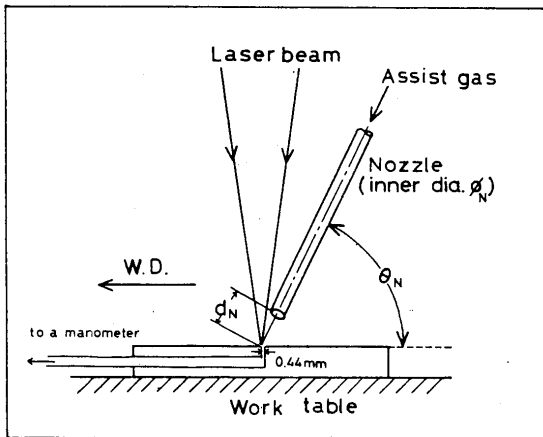
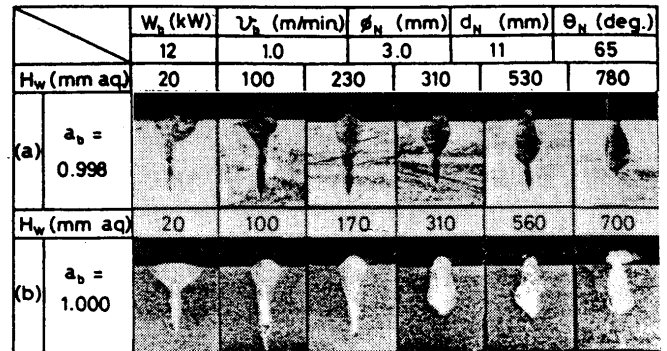|	W_b (kW)	V_b (m/min)	ϕ_N (mm)	d_N (mm)	Θ_N (deg.)
	12	1.0	3.0	11	65
H_w (mm aq)	20	100	230	310	530	780
(a) $a_b = 0.998$					
H_w (mm aq)	20	100	170	310	560	700
(b) $a_b = 1.000$					

Fig. 61 Influence of assist gas on bead shape.

10 mm

gas has a strong influence on the penetration depth, bead width and bead shape, as shown in **Fig. 60** and **Fig. 61**[66].

As the pressure of the assist gas increases, the amount of laser plasma decreases and the shape of the bead cross section changes from a wine-cup shape to an egg shape passing through a nail-head shape. A particular assist gas pressure should be selected for maximizing the penetration depth.

5.2.2.Laser spike seam welding

One of the most effective solutions for dealing with this laser plasma problem is the "Laser Spike Seam Welding" (LSSW) method invented by the author. In this process, the laser beam is oscillated so that it follows the movement of the specimen. The laser beam stops relative to the specimen for a certain period, it drills the specimen as a pulsed beam, then it quickly returns to its original point to keep away the laser plasma. **Figure 62** shows a

Fig. 59 Assist gas nossle for high power CO_2 laser welding.
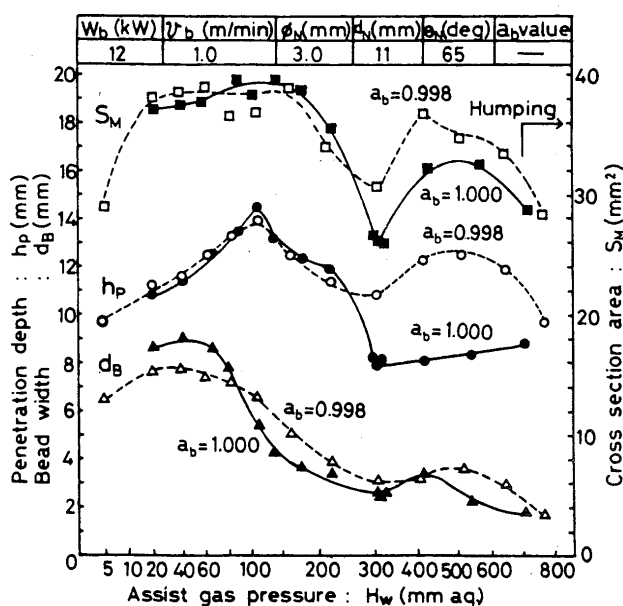
Fig. 60 Influence of assist gas on penetration depth and bead width.

a) LSSW   b) Conventional
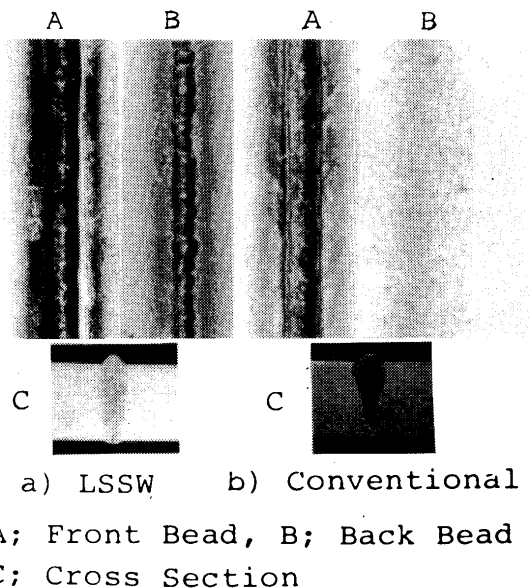
A; Front Bead, B; Back Bead

C; Cross Section

Fig. 62 Comparison of bead appearance and cross section between LSSW and conventional laser welding under the same welding conditions.
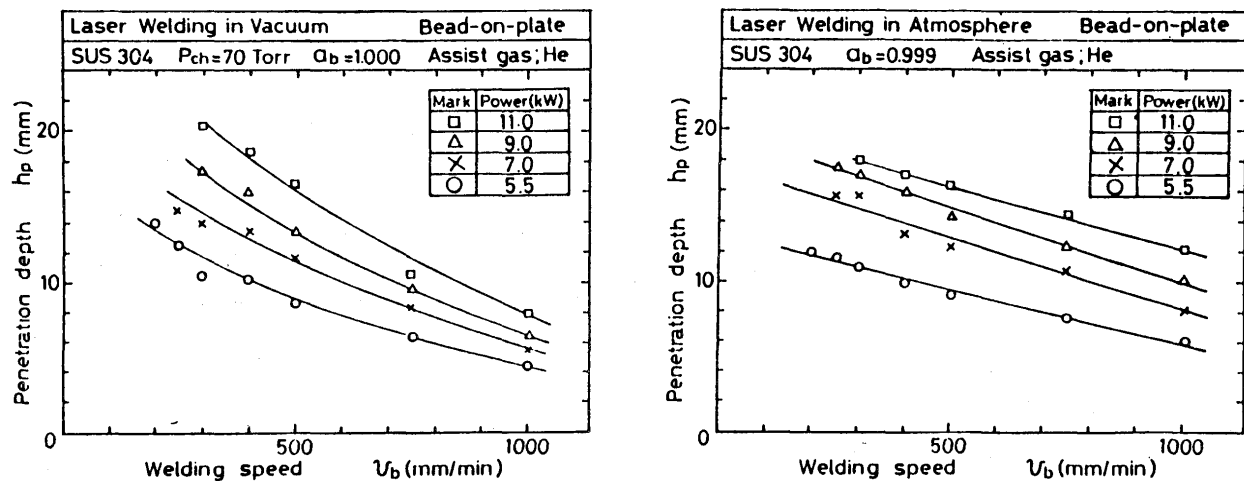
Fig. 63 Comparison of penetration depth between atmospheric and vacuum laser welding.

comparison of the bead appearance and cross section between LSSW and conventional laser welding under the same welding conditions: power, welding speed, gas flow rate etc. It can be seen that the LSSW process is superior in both the penetration depth and bead appearance[67].

5.2.3. Vacuum Laser welding

Vacuum laser welding is another solution for the problem of laser plasma. In a low vacuum of a few tens of Torr, less laser plasma is produced and the penetration depth increases with decreasing welding speed. This tendency is more evident than in atmospheric laser welding, as shown in Fig. 63[68].

5.3. Differences and similarities in processing characteristics of laser beam and electron beam

(1) The electron beam is easy to propagate and control in a vacuum, but its propagation range in air is extremely short. Particularly, its working distance for use as a heat source is too short to control, and so its working function is limited. On the other hand, the CO_2 laser beam is easy to propagate and control in air, and has good workability. However, during passage through hot gas or plasma, its energy absorption is so high that its working function is restricted. Thus, the larger the laser output the harder the plasma removal in air. However, in a vacuum, since the laser plasma disappears, the workability of these two beams (EB and LB) becomes similar. These phenomena were revealed by dynamic observation of the beam hole during actual welding[64],[69].

(2) "Bead transition" occurs in laser beams, but never in electron beams. Thus, extremely high precision is required for controlling the working distance of laser

beams.

(3) Laser beams have a particularly high reflection coefficient to metallic materials. Although the energy absorption rate of laser beams is not so high, it can be high to surface oxidation, non-metallic coating or non-metallic material. An electron beam causes a charge-up to non-metallic materials.

(4) Electrical power efficiency of beam generation is high for the electron beam but low for the laser beam. However, the latter generally has a better working performance in air.

(5) In electron beam welding, the thicker the plate the more effective the welding characteristics, but in the case of laser beam, the weldable plate thickness is limited practically, on the contrary, the laser beam is more suitable for cutting.

(6) Concerning surface treatment, each of the two beams has respective advantages and disadvantages.

References

1) J.R. Pierce; J. App. Phys., 11 (1940).

2) K.H. Steigerwald; Verhandl. deut. Physik., Gas, 4, 123 (1953).

3) J.A. Stohr; Fuel Elements Conference, Paris, November, 18-23 (1957).

4) T.H. Maiman; Nature, Vol. 187 (1960).

5) C.K.N. Patel; Phys. Rev., 136-5A (1964).

6) W.B. Bridges; Appl. Phys. Lett., 4-128 (1964).

7) M. Okada, Y. Arata, K. Nishiguchi and H. Maruo; Reports in the First Symposium of Atomic Energy in Japan, 1, 409 (1957).

8) Y. Arata; Chokoon Kenkyu, 1-6 (1957).

9) M. Okada and Y. Arata; Tech. Report of Osaka Univ., 13-567 (1963).

10) Y. Arata and M. Tomie; Trans. of JWRI, 2-1 (1973).

11) Y. Arata and M. Tomie; Journal of JWS, 46-7 (1977).

12) Demonstration of the Research Center for Ultra High Energy Density Heat Source in JWRI, October (1980).

13) Y. Arata and M. Tomie; Journal of High Temperature Society, 10-3 (1984).

14) Y. Arata and M. Tomie; Trans. of JWRI, 2-1 (1973), 4-1 (1975), 5-1 (1976); IIW. Doc VI-112-73 (1973); 2nd International Symposium of JWS, (1975); 7th International Conference of Electron and Ion Beam Science and Technology (at Washington, D.C., USA) (1976); Proc. of Inter. Conf. on Welding Research in 1980's, Poster Session, October (1980) (at JWRI).
A. Sanderson; Metal Construction BWJ, 6-1 (1974).
G. Sayagh, P. Dumonte and T. Nakamura; 2nd International Symposium of JWS, (1975).
K.S. Akop' yant, et al.; Automatic Welding, 28-4 (1975).

15) D.R. Whitehouse; Contract No. DA-01-021-AMC-12427(z).

16) W.B. Tiffany, R. Targ and J.D. Foster; App. Phys. Lett. 15-3 (1969).

17) E.V. Locke; E.D. Hoag and R.A. Hella; IEEE Quantum Electronics, QE-8-2 (1972).

18) C.M. Banas; Final report under Naval Research Laboratories Contract N00173-76-M-0107, UTRC. Report, No. R76-912260-1, August (1976).

19) Y. Arata and I. Miyamoto; Tech. Report of Osaka Univ., 17-285 (1967).

20) Y. Arata and M. Tomie; Trans. of JWS, 1-2 (1970).

21) H. Maruo, I. Miyamoto and Y. Arata; Proc. 1st Int. Laser Processing Conf. (1981); Proc. Annual Meeting of JWS (in Japanese) (1978).

22) H. Maruo, I. Miyamoto, T. Ishida and Y. Arata; Proc. 1st Int. Laser Processing Conf. (1981).

23) S. Katayama, A. Matsunawa, A. Morimoto, S. Ishimoto and Y. Arata; Proc. 3rd CISFFEL (1983).

24) Y. Arata; J. Phys. Japan 43-3 (1977).

25) Y. Arata and I. Miyamoto; Tech. Report of Osaka Univ., 19-887 (1967).; Y. Arata, I. Miyamoto and M. Kubota; IIW Doc. IV-4-69 (1969).

26) Y. Arata and I. Miyamoto; Trans. of JWS, 3-1 (1972).

27) AVCO HPL Lasers Tech. Note, No. 6 (1977).; R.M. Feinberg; Proc. Int. Conf. on Welding Research in the 1980's (1980).

28) Y. Arata; Journal of JWS, 41-11 (1972).

29) Y. Arata, M. Tomie and Y. Kato; Trans. of JWRI, 2-1 (1973).

30) Y. Arata, T. Ishimura and I. Miyamoto; Trans. of JWRI, 2-1 (1973).

31) Y. Arata, K. Inoue, H. Maruo and I. Miyamoto; Lectures of the International "Beam Technologegy" Conference in Essen on the 7th and 8th, May (1980) DVS-BERICHTE.

32) Y. Arata, H. Maruo, I. Miyamoto and F. Kawabata; Journal of JWS, 49-10 (1980).

33) A. Sanderson; British Welding Journal, 15-10 (1968).

34) P. Bwmonte et al.; IIW Doc. IV-131-73 (1973).

35) G. Sayagh; IIW Doc. IV-276-79 (1979).

36) Y. Arata, M. Tomie, H. Nagai and T. Hattori; Trans. of JWRI, 2-2 (1973).

37) H. Irie, T. Hashimoto and M. Inagaki; Journal of JWS, 46-9 (1977).

38) Y. Arata and I. Miyamoto; Journal of JWS, 39-12 (1970).

39) Y. Arata and I. Miyamoto; Trans. JWS, 3-1 Report 1 (1972).

40) E. Hagen and H. Rubens; Ann. Physik, 11 (1903).

41) Y. Arata and I. Miyamoto; Trans. JWS, 3-1, Report 2 (1972); Trans. of JWRI, 2-2 (1973).

42) Y. Arata and I. Miyamoto; Second Int. Symp. of JWS, (1975).

43) A.A. Wells; Weld. J., 22-5 (1952).

44) Y. Arata and K. Inoue; Trans. of JWRI, 2-1 (1973).

45) Y. Arata and I. Miyamoto; Trans. of JWRI, 1-1 (1972).

46) Y. Arata and M. Tomie; Journal of JWS, 46-8 (1977).

47) M.J. Adams; Brit. Weld. J., 15-3 (1968).

48) A. Sanderson; Brit. Weld. J., 15-10 (1968).

49) Kawasaki Heavy Industries Ltd., Private communication.

50) Y. Arata, M. Ohsumi and Y. Hayakawa; Trans. of JWRI, 5-1 (1976).

51) E.L. Locke, E.D. Hoag and R.A. Hella; IEEE Quantum Electronics QE-8-2 (1972).

52) Y. Arata, H. Maruo and I. Miyamoto; IIW. Doc. IV-241-78 (1978); 212-436-78 (1978).

53) Y. Arata, F. Matsuda and K. Nakata; Trans. of JWRI, 1-1 (1972); 2-1 (1973).

54) M.J. Bibby, J.A. Goldak and G. Burbidge; Weld. J., 54-8 (1975).

55) Y. Arata, N. Ohji, N. Kohsai and K. Nishiguchi; 2nd Int. Colloq. for EBW and Melting (1978); IIW. Doc. IV-263-79 (1979); Trans. of JWRI, 8-1 (1979).

56) J. Dearden and H.O. Neill; Trans. Inst. Weld. (U. K.), 1-3 (1940).

57) H. Kihara, H. Suzuki and H. Tamura; IIW Doc. No. 1, IX-288-61 (1961).

58) Y. Arata, Y. Shibata and S. Fujihira; Trans. of JWRI, 3-2 (1974); 4-2 (1975).; Y. Arata; Journal of SMS, 27-301 (1978).

59) Y. Arata and M. Tomie; 2nd International Symposium of JWS, (1975).

60) Y. Arata and M. Tomie; Trans. of JWRI, 9-2 (1980).

61) K. Shinada, Y. Kondo, S. Satoh, T. Shimoyama, G. Takano, M. Minami, T. Tanaka and Y. Arata; Proc. Int. Conf. on Welding Research in the 1980's (1980).

62) Y. Arata and E. Nabegata; Trans. of JWRI, 7-1 (1978).

63) Y. Arata, E. Nabegata and N. Iwamoto; Trans. of JWRI, 7-2 (1978).

64) Y. Arata, N. Abe and S. Yamamoto; Trans. of JWRI, 9-1 (1980).

65) Y. Arata, N. Abe, H. Wang and E. Abe; Trans. of JWRI, 11-2 (1982).

66) Y. Arata, T. Oda and R. Nishio; Trans. of JWRI, 12-2 (1983).

67) Y. Arata, N. Abe and T. Oda; Proc. ICALEO'83 (1983).

68) Y. Arata and T. Oda; Journal of High Temperature Society, 10-1 (1984).

69) Y. Arata; What Happens in High Energy Density Welding and Cutting?, 1980).